

Supplementary information for
UV to NIR multistate electrochromism and
electrofluorochromism in dibenzophenazine-arylamine
derivatives

Bahadur Sk,^{a,‡} Madhurima Sarkar,^{a,‡} Kuldeep Singh,^a Arunava Sengupta^b and Abhijit Patra^{a,*}

^aDepartment of Chemistry, Indian Institute of Science Education and Research Bhopal,
Bhopal Bypass Road, Bhauri, Bhopal 462066, Madhya Pradesh, India

Email: abhijit@iiserb.ac.in

^bDepartment of Chemistry, Indian Institute of Technology Kanpur, Kanpur,
Uttar Pradesh, 208016, India

Sr. no	Contents	Page no.
I	Materials and methods	S2
a	Chemicals	S2
b	Instrumentation	S2-S3
II	Design strategy	S4
III	Synthesis and characterization	S5-S7
IV	Spectroscopic study	S8
a	Electronic absorption	S8
b	Steady-state emission	S9
c	Lippert-Mataga plot	S10-S11
d	Fluorescence quantum yield and lifetime	S11-S12
e	Spectroscopic data table	S12
V	Cyclic voltammetry	S13-S14
VI	Electrochemical stability of PMDPA and PMTPA	S15-S16
VII	Cathodic electrochromic properties of PMDPA	S17
VIII	Chemical oxidation of PMDPA and PMTPA by SbCl ₅	S18
a	UV-Vis-NIR absorption	S18-S19
b	IVCT analysis	S19
IX	Electron paramagnetic resonance (EPR) of D-A-D compounds	S20
X	Electrofluorochromism of PMDPA and PMTPA	S20-S22
XI	Computational investigations	S23-S25
XII	EC-EFC switching of the PMDPA thin film	S26-S27
XIII	Characterization: ¹ H NMR, ¹³ C NMR and Mass spectra	S28-S33
XIV	References	S34-S35

I. Materials and methods

(a) Chemicals:

All chemicals were used as received unless otherwise stated. 9,10-phenanthrenequinone (99%), 3,4-diaminobenzophenone (97%), diphenylamine (99%), 4-bromotriphenylamine (97%), *N*-bromosuccinimide (99%), bis(pinacolato)diboron (99%), palladium(II) acetate (99.9%), tris(dibenzylideneacetone)dipalladium(0) (97%), X-Phos (98%), potassium *tert*-butoxide (99%), 1,1'-bis(diphenylphosphino)ferrocenedichloropalladium(II) (99%), tetrakis(triphenylphosphine)palladium(0) (99.9%), tetra-*n*-butylammonium bromide (98%), antimony(V) chloride (99%), tetrabutylammonium hexafluorophosphate (99%), toluene (99.85%), dimethyl sulfoxide (99%) were purchased from Sigma-Aldrich. Potassium carbonate, sulphuric acid (concentrated), acetic acid, chloroform and 1,4-dioxane were received from Merck. Tetrahydrofuran (99%), dichloromethane, ethanol (99.8%) were received from Spectrochem.

(b) Instrumentation:

Bruker Avance III NMR spectrometer was used for recording the ^1H and ^{13}C -NMR spectra. Bruker MicrOTOF-Q-II mass spectrometer was used for obtaining high-resolution mass spectrometry (HRMS) data. Melting points of the D-A-D compounds were determined using a digital melting point apparatus (Jyoti: AN ISO: 9001:2000, India). Compounds were taken into the glass capillary for measurements. Cary 100 absorption spectrophotometer was used for recording the UV-Vis absorption spectra. On the other hand, for recording the UV-Vis-NIR absorption spectra, Cary 5000 UV-Vis-NIR absorption spectrophotometer was used. The steady-state and time-resolved fluorescence spectra were recorded using Jobin Yvon Horiba Model Fluorolog-3-21 and time-correlated single-photon counting (TCSPC) spectrometer (Delta Flex-01-DD), respectively. Delta diode laser of 468 and 510 nm were used as the excitation source. For decay curve analysis, IBH DAS6 (version 6.8) software was used. The fitting quality was assessed by χ^2 and the visual inspection of the residuals.

Cyclic Voltammetry: All the cyclic voltammetry measurements were carried out in deoxygenated dichloromethane (DCM) with 0.1 M tetrabutylammonium hexafluorophosphate (TBAP) as supporting electrolyte in a three-electrode system using BioLogic SP300 potentiostat (BioLogic, France). Glassy carbon (GC) was used as a working electrode, platinum wire (Pt) and Ag/AgCl were used as counter and reference electrodes, respectively. The scan rate was kept at 100 mV/s for all the measurements.

Spectroelectrochemical measurements: Spectroelectrochemical measurements were carried out in an electrochemical workstation (model: 600B series) from CH instruments. The change in the optical absorption in response to electric potential was monitored in a custom-made cell,

Model EF-1350 (Bioanalytical Systems Inc., U.S.A), consisting of a Pt mesh electrode, a Pt wire, and Ag/AgCl as working, counter, and reference electrode, respectively. Deoxygenated dichloromethane solution containing the active compounds and 0.1 M TBAP as supporting electrolyte was taken into the spectroelectrochemical cell for the measurements.

Electrofluorochromism experiments: The electrofluorochromism experiments were carried out in a typical fluorescence spectroelectrochemical cell equipped with a platinum mesh, a platinum wire, and Ag/AgCl as working, counter, and reference electrode, respectively. The spectroelectrochemical cell containing the electroactive compounds and 0.1 M TBAP as supporting electrolyte in dichloromethane was placed in the sample compartment of a spectrofluorometer. The response of electric potential on emission signals was monitored in a double potential step chronoamperometry experiment.

II. Design strategy

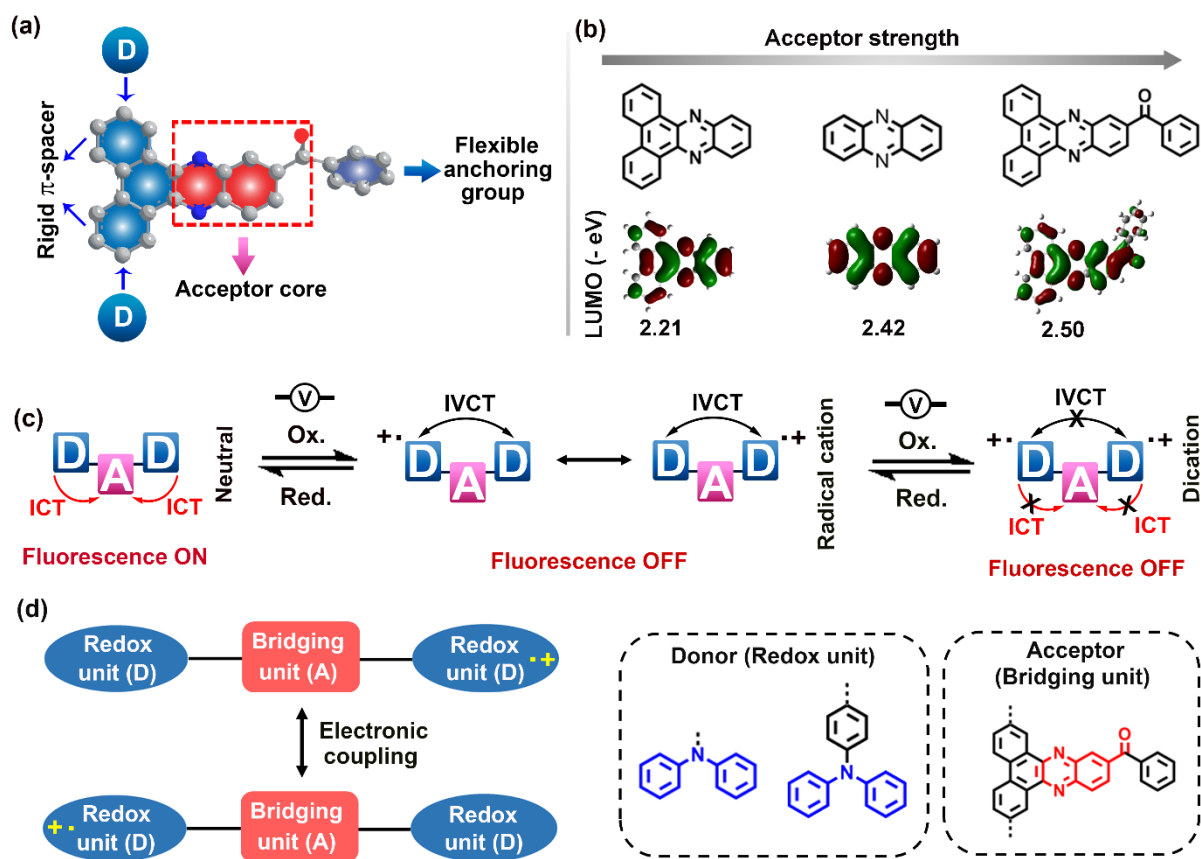
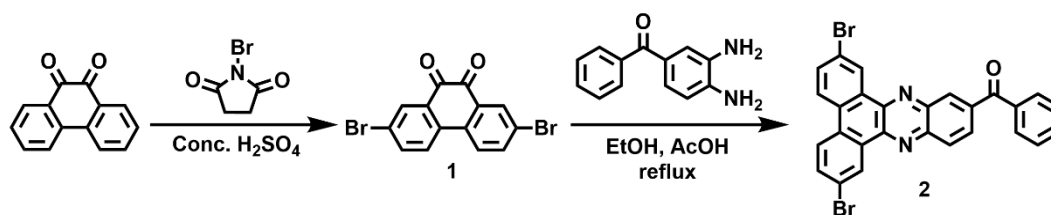


Fig. S1 (a) Schematic illustration of design strategy representing the salient features of donor-acceptor-donor (D-A-D) architecture involving dibenzo[*a,c*]phenazin-11-yl(phenyl)methanone (PM) as an acceptor unit. (b) Electron density distribution in LUMO levels of dibenzophenazine, phenazine, and dibenzo[*a,c*]phenazin-11-yl(phenyl)methanone estimated using B3LYP/6-31G(d,p). (c) Electron oxidation (Ox.) / reduction (Red.) pathways of D-A-D compound representing intramolecular charge transfer (ICT) and intervalence charge transfer (IVCT) responsible for electro-tunable absorption and fluorescence. (d) Schematic representation indicating the electronic coupling in mixed-valence compounds using dibenzo[*a,c*]phenazin-11-yl(phenyl)methanone as a bridging unit and diphenylamine and triphenylamine as the redox units.

The intramolecular charge transfer (ICT) in a donor-acceptor-based multichromophoric system is highly sensitive towards external stimuli such as electric potential.¹⁻³ Herein, dibenzo[*a,c*]phenazin-11-yl(phenyl)methanone (PM) was chosen as the central acceptor unit for designing the donor-acceptor-donor-based electrochromic-electrofluorochromic materials considering the lower LUMO energy level compared to dibenzophenazine and phenazine (Fig. S1). The effect of intramolecular and intervalence charge transfer (IVCT) to facilitate UV to NIR electrochromism and tunable electrofluorochromism in donor-acceptor-donor-based mixed-valence systems was elucidated. Additionally, the impact of electronic coupling in mixed-valence systems was investigated, varying the redox-active donor units. We could demonstrate a new donor-acceptor-based small organic molecule exhibiting stable multistate electrochromism and electrofluorochromism.

III. Synthesis and characterization



Scheme S1 Schematic illustration of the synthesis pathway of 2,7-dibromodibenzo[*a,c*]phenazin-11-yl(phenyl)methanone (**2**).

2,7-dibromodibenzo[*a,c*]phenazin-11-yl(phenyl)methanone (**2**) was synthesized via a two-step process by following a reported method (Scheme S1).^{4,5}

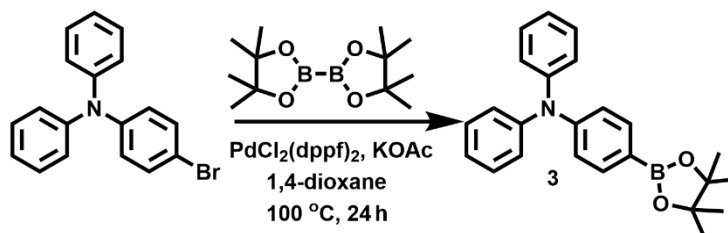
Synthesis of 2,7-dibromophenanthrene-9,10-dione (1): The bromination was carried out by the addition of *N*-bromosuccinimide (1 g, 2.5 eqv.) to a solution of phenanthrene-9,10-dione (500 mg, 1 eqv.) in 98% H₂SO₄ while stirring for 3 h at room temperature. The yellowish-orange reaction mixture was quenched with ice-cold water. The colored product was filtered out and washed with water. The dry crude product was recrystallized in dimethyl sulfoxide (DMSO) to obtain the pure 2,7-dibromophenanthrene-9,10-dione (**1**) with 75% yield (Scheme S1).

¹H NMR (500 MHz, DMSO-*d*₆, δ): 8.26 (d, $J = 8.6$ Hz, 2H), 8.08 (d, $J = 2.3$ Hz, 2H), 7.97 (dd, $J = 8.5, 2.3$ Hz, 2H).

Synthesis of 2,7-dibromodibenzo[*a,c*]phenazin-11-yl(phenyl)methanone (2): 3,4-diaminobenzophenone (1 eqv.) and compound **1** (1 eqv.) were dissolved in ethanol. A catalytic amount of acetic acid was added to the solution, and the mixture was kept for 6 h under the refluxing condition. The reaction mixture was then brought to room temperature and filtered. The solid residue was washed with water followed by ethanol to get product **2** as a yellow solid (80% yield, Scheme S1).

¹H NMR (500 MHz, CDCl₃, δ): 9.54 (d, $J = 2.1$ Hz, 1H), 9.47 (d, $J = 2.1$ Hz, 1H), 8.69 (d, $J = 1.5$ Hz, 1H), 8.46 (d, $J = 8.7$ Hz, 1H), 8.39 (m, 1H), 8.37 (m, 2H), 7.97 (m, 2H), 7.91 (m, 2H), 7.71 (m, 1H), 7.60 (m, 2H).

Synthesis of *N,N*-diphenyl-4-(4,4,5,5-tetramethyl-1,3,2-dioxaborolan-2-yl)aniline (3):

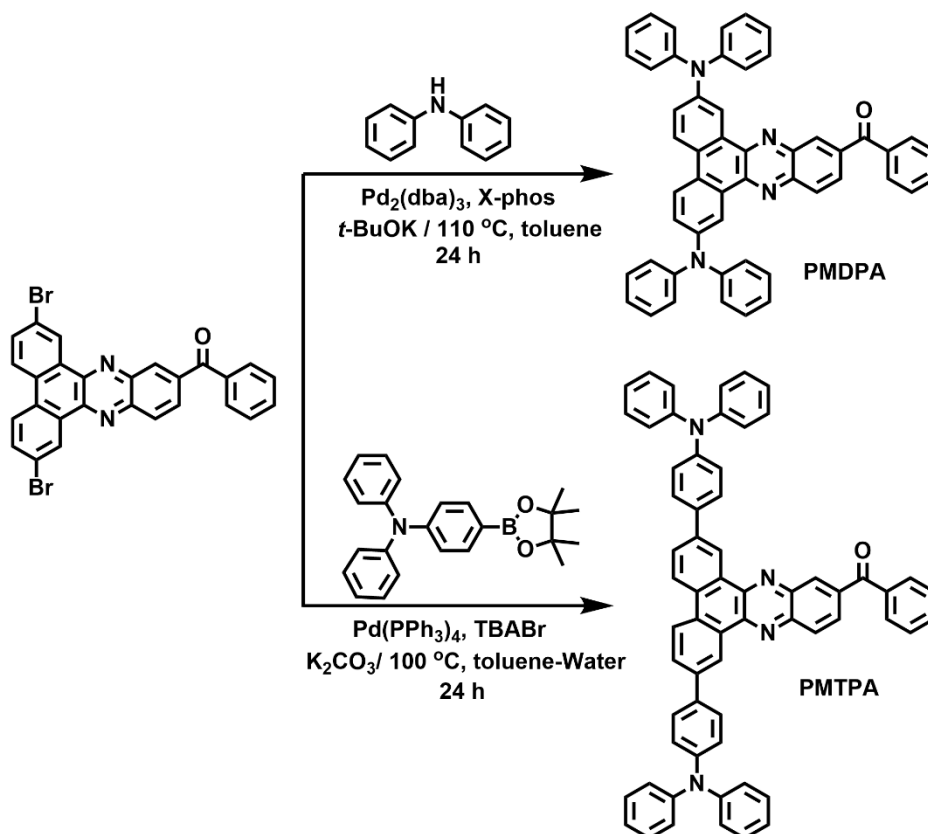


Scheme S2 Synthetic pathway of *N,N*-diphenyl-4-(4,4,5,5-tetramethyl-1,3,2-dioxaborolan-2-yl)aniline (**3**).

The synthesis of *N,N*-diphenyl-4-(4,4,5,5-tetramethyl-1,3,2-dioxaborolan-2-yl)aniline (**3**) was carried out by following a reported procedure.⁶ Firstly, 4-bromotriphenylamine, bis(pinacolato)diboron, [1,10-bis-(diphenylphosphino)-ferrocene]dichloropalladium, potassium acetate were added in a Schlenk tube. N₂/vacuum cycle was carried out multiple times. Dry 1,4-dioxane (10 mL) was added to the mixture, and it was kept for stirring at 100 °C for 24 h. The reaction mixture was quenched with water. After that, the product was extracted with dichloromethane, followed by drying over the anhydrous magnesium sulfate (MgSO₄). A flash column (silica gel) using hexane/DCM (V/V, 4:1) as the eluent led to a pure solid white product, **3**. (60% yield, Scheme S2).

¹H NMR (500 MHz, CDCl₃, δ): 7.72 – 7.66 (m, 2H), 7.30 – 7.26 (m, 4H), 7.13 (m, 4H), 7.09 – 7.04 (m, 4H), 1.36 (s, 12H). ¹³C NMR (126 MHz, CDCl₃, δ): 150.99, 147.79, 136.24, 129.69, 125.39, 123.75, 122.19, 83.96, 25.26.

Synthesis of PMDPA and PMTPA:



Scheme S3 Synthetic schemes of PMDPA and PMTPA.

Synthesis of (2,7-bis(diphenylamino)dibenzo[*a,c*]phenazin-11-yl)(phenyl)methanone (PMDPA): A mixture of (2,7-dibromodibenzo[*a,c*]phenazin-11-yl)(phenyl)methanone (**2**) (1 eqv.), diphenylamine (2.2 eqv.), Pd₂(dba)₃ (0.05 eqv.), *t*-BuOK (2.5 eqv.) and X-Phos (0.05 eqv.) were added in a Schlenk tube. After that, N₂/vacuum cycle was carried out multiple times.

Toluene (10 mL) was added to the mixture and was kept for stirring at 110 °C for 24 h under a nitrogen atmosphere. The reaction was quenched with water. The product was extracted with DCM followed by drying over MgSO₄. Column chromatography (neutral alumina, 4.5 : 5.5, DCM : hexane, V/V) purification followed by multiple re-precipitation in dichloromethane/methanol (4:1) led to pure PMDPA (53% yield, m.pt.: 295 °C, Scheme S3). The compound was characterized by ¹H, ¹³C NMR spectroscopy, and mass spectrometry.

¹H NMR (500 MHz, CDCl₃, δ): 9.06 (d, *J* = 2.5 Hz, 1H), 9.00 (d, *J* = 2.5 Hz, 1H), 8.54 (d, *J* = 1.7 Hz, 1H), 8.31 (d, *J* = 8.8 Hz, 2H), 8.28 (d, *J* = 8.8 Hz, 1H), 8.21 (m, 1H), 7.92 – 7.89 (m, 2H), 7.65 (m, 1H), 7.54 (d, *J* = 13.3 Hz, 2H), 7.49 (m, 2H), 7.32 (m, 8H), 7.22 (m, 8H), 7.09 (m, 4H). **¹³C NMR (126 MHz, CDCl₃, δ):** 196.02, 147.57, 147.55, 147.20, 147.14, 143.78, 143.52, 143.43, 140.90, 137.87, 137.27, 132.85, 132.64, 130.55, 130.24, 129.91, 129.50, 129.45, 129.27, 128.54, 127.39, 127.29, 127.25, 127.12, 124.62, 124.40, 123.91, 123.35, 123.22, 120.05, 119.86. **HRMS (APCI):** calculated for C₅₁H₃₄N₄O is 718.27 and found 719.2789 [M+H⁺].

Synthesis of (2,7-bis(4-(diphenylamino)phenyl)dibenzo[*a,c*]phenazin-11-yl)(phenyl)methanone (PMTPA): A mixture of (2,7-dibromodibenzo[*a,c*]phenazin-11-yl)(phenyl)methanone (**2**) (1 eqv.), *N,N*-diphenyl-4-(4,4,5,5-tetramethyl-1,3,2-dioxaborolan-2-yl)aniline (**3**) (2.1 eqv.), K₂CO₃ (1 eqv.), tetrabutylammonium bromide (0.09 eqv.) and tetrakis(triphenylphosphine)-palladium(0) (0.03 eqv.) were taken in a Schlenk tube. An inert atmosphere was maintained through multiple N₂/vacuum cycles. Degassed water (2 mL) and toluene (10 mL) were added to the mixture, and it was kept for stirring at 100 °C for 24 h. The reaction mixture was quenched with water. The product was extracted with dichloromethane followed by drying over MgSO₄. Column chromatography (neutral alumina, 3 : 7, DCM : hexane, V/V) purification followed by multiple re-precipitation in dichloromethane/methanol (4:1) led to pure PMTPA (45% yield, m.pt.: 150 °C, Scheme S3). The compound was characterized by ¹H, ¹³C NMR spectroscopy, and mass spectrometry.

¹H NMR (500 MHz, CDCl₃, δ): 9.66 (d, *J* = 1.9 Hz, 1H), 9.58 (d, *J* = 1.9 Hz, 1H), 8.72 (s, 1H), 8.62 (d, *J* = 9.1 Hz, 2H), 8.47 (d, *J* = 8.7 Hz, 1H), 8.37 (d, *J* = 10.0 Hz, 1H), 8.06 (m, 2H), 7.98 (d, *J* = 8.1 Hz, 2H), 7.79 (m, 4H), 7.67 (m, 1H), 7.59 (m, 2H), 7.34 – 7.27 (m, 9H), 7.23 – 7.15 (m, 11H), 7.07 (m, 4H). **¹³C NMR (126 MHz, CDCl₃, δ):** 196.13, 147.77, 147.75, 143.92, 141.18, 140.16, 138.00, 137.60, 134.12, 133.20, 132.94, 130.76, 130.38, 130.27, 129.52, 129.50, 129.15, 128.73, 128.16, 128.12, 124.76, 124.74, 124.32, 123.99, 123.95, 123.71, 123.31, 123.28. **HRMS (APCI):** calculated for C₆₃H₄₂N₄O is 870.34 and found 871.3461 [M+H⁺].

IV. Spectroscopic study

(a) Electronic absorption:

The absorption spectra of D-A-D compounds (PMDPA and PMTPA) were compared with that of their precursor units (donor and acceptor unit) in toluene (Fig. S2). The main absorption peak for PMDPA and PMTPA arising at 365-370 nm (π - π^* transition) was due to the donor diphenylamine (DPA) and triphenylamine (TPA) units, respectively, while a small hump could be seen at 400-410 nm for the PM acceptor unit. A broad absorption band at 520 and 465 nm was observed for PMDPA and PMTPA, respectively, due to the donor to acceptor intramolecular charge transfer. No significant change of peak maxima and shape was found in the absorption spectra of D-A-D compounds with varying solvent polarity.

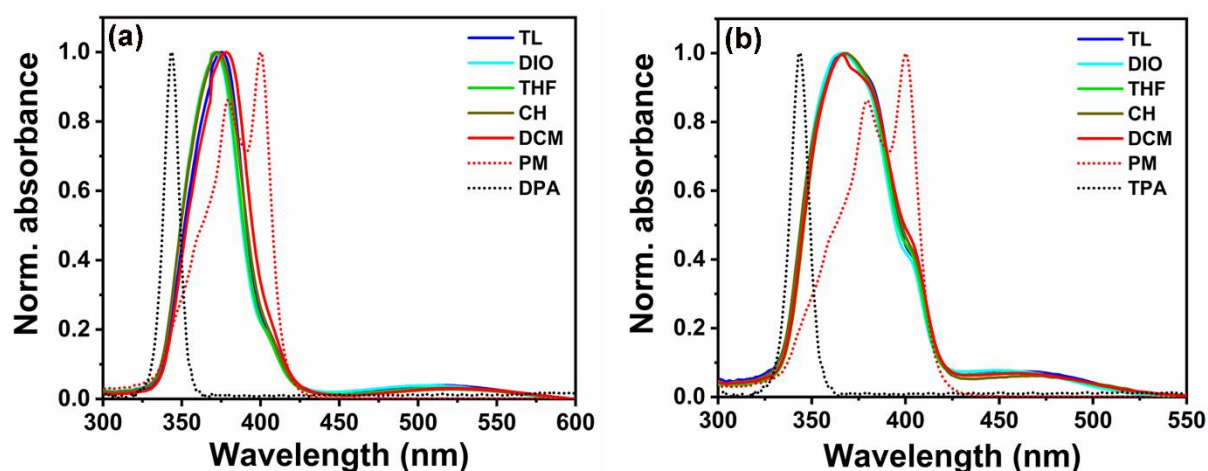


Fig. S2 Normalized absorption spectra (solid line) of (a) PMDPA and (b) PMTPA in the various polar solvents; TL: toluene, DIO: 1,4-dioxane, THF: tetrahydrofuran, CH: chloroform, and DCM: dichloromethane. Normalized absorption spectra (dotted line) of the acceptor (PM) and the respective donor (DPA, TPA) units in TL were shown for comparison.

Table S1 Molar absorption coefficients (ϵ) of PMDPA and PMTPA in DCM at π - π^* and ICT bands.

Compounds	Absorption bands (nm)	
	π - π^* (ϵ , $M^{-1} cm^{-1}$)	ICT (ϵ , $M^{-1} cm^{-1}$)
PMDPA	370 (71,000)	520 (2990)
PMTPA	365 (93,000)	465 (8240)

(b) Steady-state emission:

The steady-state emission spectra of PMDPA and PMTPA were recorded in different solvents with varying polarity. Both the compounds showed a broad emission band in all the solvents Fig. S3. Red-shifted emission with large Stokes shift was observed in nonpolar solvent, toluene to polar solvent, dichloromethane. The significant Stokes shifts and spectral broadening in the polar solvents indicated a highly polarized ICT state.

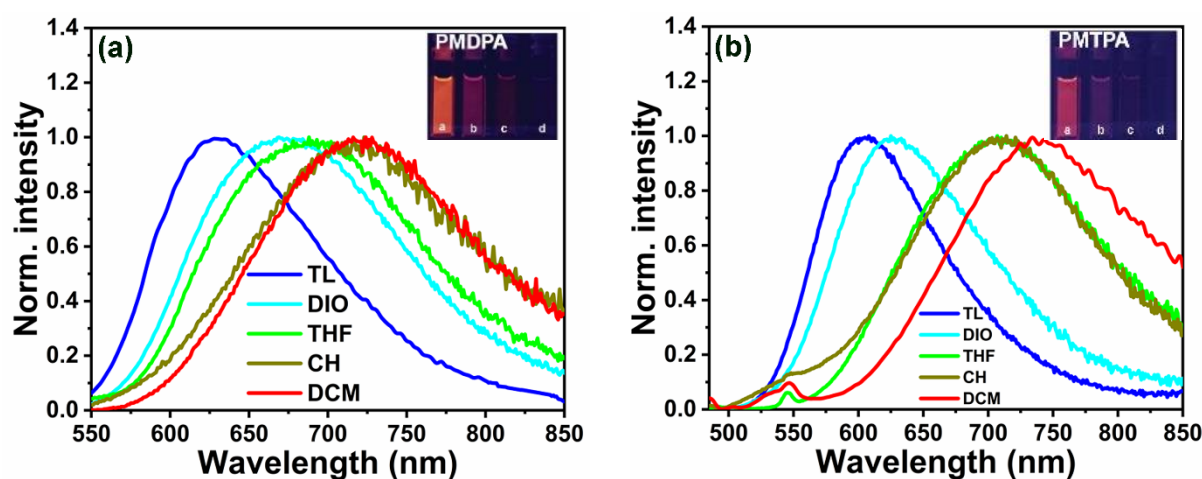


Fig. S3 Normalized emission spectra of (a) PMDPA ($\lambda_{\text{ex}} = 520$ nm), and (b) PMTPA ($\lambda_{\text{ex}} = 465$ nm) in the solvents of varied polarity; TL: toluene, DIO: 1,4-dioxane, THF: tetrahydrofuran, CH: chloroform and DCM: dichloromethane. Inset: digital photographs of PMDPA and PMTPA in (a) TL, (b) DIO, (c) THF, (d) DCM under 365 nm UV lamp.

Further, the excitation spectra obtained at respective emission maxima of D-A-D compounds in different polar solvents were comparable with the corresponding absorption spectra (Fig. S4).

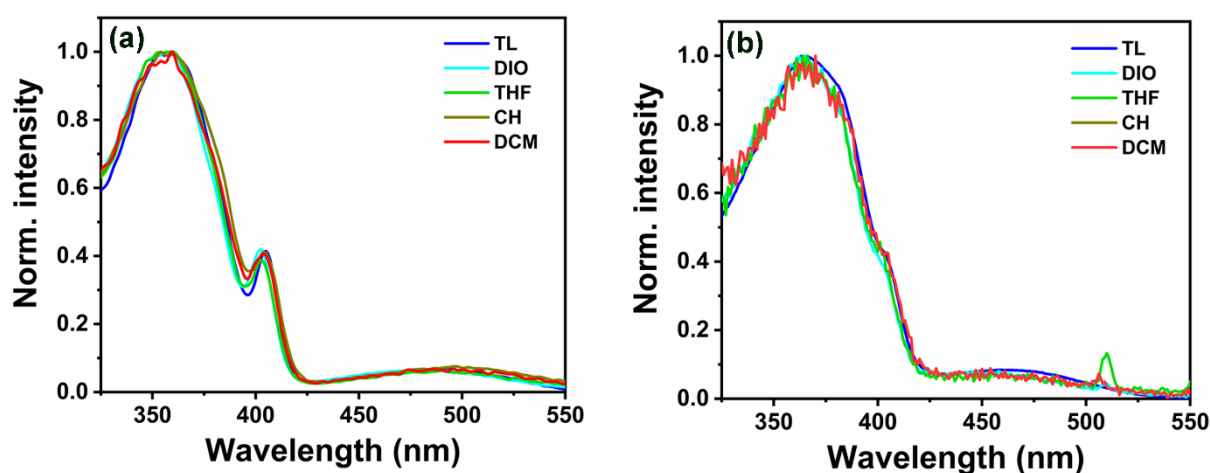


Fig. S4 Normalized excitation spectra of (a) PMDPA and (b) PMTPA at respective emission maxima in different polar solvents; TL: toluene, DIO: 1,4-dioxane, THF: tetrahydrofuran, CH: chloroform and DCM: dichloromethane.

(c) Lippert-Mataga plot:

The solvent dependence spectral shifts were analyzed using the Lippert-Mataga equation, as mentioned below.⁷

$$\Delta\bar{\nu} = \bar{\nu}_a - \bar{\nu}_f = \frac{2}{hc} \left(\frac{\epsilon - 1}{2\epsilon + 1} - \frac{n^2 - 1}{2n^2 + 1} \right) \frac{(\mu_E - \mu_G)^2}{a^3} + constant \quad \dots \text{ (S1)}$$

$$\text{where: } \bar{\nu}_a = \frac{1}{\lambda_{abs}^{max}}, \bar{\nu}_f = \frac{1}{\lambda_{em}^{max}} \quad \text{and } \Delta f = \left(\frac{\epsilon-1}{2\epsilon+1} - \frac{n^2-1}{2n^2+1} \right) \quad \dots \text{ (S2)}$$

Eq. S.1 shows that the Stokes shift ($\Delta\bar{\nu}$) depends on the dipole moments at ground state (μ_G) and excited state (μ_E) of the fluorophore and the nature of the polar solvent such as the dielectric constant (ϵ) and the refractive index (n). $\bar{\nu}_a$ and $\bar{\nu}_f$ represent the wavenumbers of the absorption maxima and the emission maxima, respectively, h is the Planck's constant, c is the speed of light in vacuum, and a is the Onsager radius of the cavity in which the fluorophore resides. Δf is the orientation polarizability of the solvent (Eq. S.2). Plotting the Stokes shift with respect to the orientation polarizability of the solvents gives the Lippert-Mataga plot.^{7,8}

A relation between solvent polarity parameter E_T^N and Stokes shift ($\Delta\bar{\nu}$) was also established. To define the solvent polarity E_T (30) / E_T^N scale is used (Eq. 1.3).⁹ E_T (30) is defined as molar electronic transition energies (E_T) of dissolved pyridinium *N*-phenolate betaine dye measured in kcal mol⁻¹ at 25 °C and 1 bar pressure.

$$E_T(30)(Kcal \text{ mol}^{-1}) = hc\bar{\nu}_{max}N_A \dots \text{ (S3)}$$

where N_A is Avogadro's number, and $\bar{\nu}$ is the electronic transition energy in wavenumber. E_T^N is the normalized value for which water and tetramethylsilane (TMS) are used as extreme polar and nonpolar reference solvents, respectively.

$$E_T^N = \left(\frac{E_T(\text{solvent}) - E_T(\text{TMS})}{E_T(\text{water}) - E_T(\text{TMS})} \right) \quad \dots \text{ (S4)}$$

Table S2 Solvent polarity parameters E_T^N , dielectric constants (ϵ), refractive indices (n), orientation polarizabilities (Δf) of different solvents and the Stokes shift ($\Delta\bar{\nu}$) of PMDPA and PMTPA are shown.

Solvents					Stokes shift, $\Delta\bar{\nu}$ (cm ⁻¹)	
Entry	E_T^N	ϵ	n	Δf	PMDPA	PMTPA
Toluene	0.099	2.38	1.497	0.013	3357	4921
1,4-dioxane	0.164	2.25	1.4224	0.024	4415	5393
THF	0.207	7.58	1.407	0.210	4701	7137
Chloroform	0.259	4.81	1.446	0.148	5195	7290
DCM	0.309	8.93	1.424	0.217	5551	7763

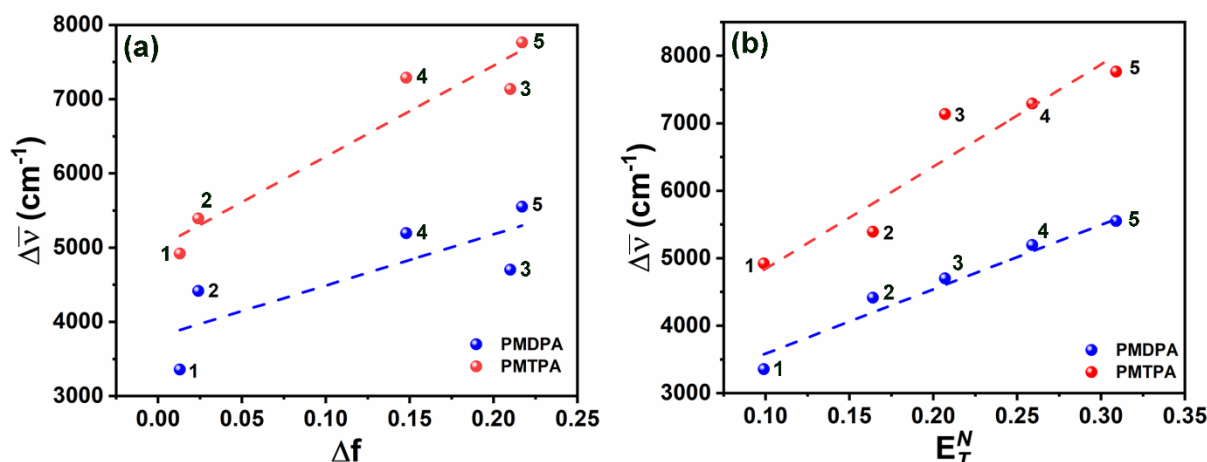


Fig. S5 (a) Lippert-Mataga plot depicting Stokes shift ($\Delta\bar{\nu}$) versus the solvent orientation polarizability (Δf) and (b) Reichardt's plot depicting Stokes shift ($\Delta\bar{\nu}$) of PMDPA and PMTPA. The dot refers to the solvents: (1) toluene, (2) 1,4-dioxane, (3) tetrahydrofuran, (4) chloroform, and (5) dichloromethane. The dashed line represents the linear fit to the data points.

The Stokes shift of all compounds showed a linear response with respect to the solvent orientation polarizability Δf (Fig. S5). $\Delta\mu$ was estimated using the Eq. S5 from the slope obtained in Fig. S5a.

$$(\mu_E - \mu_G)^2 = \frac{\text{Slope} * (hca^3)}{2} \quad \dots \text{ (S5)}$$

$\Delta\mu (\mu_E - \mu_G)$ is the change of dipole moment from the ground to the excited state. Onsager radius (a) was calculated from the geometry optimized structure of the compounds using DFT energy minimization in Gaussian program using B3LYP functional and 6-31G (d,p) basis set (*vide infra*). PMTPA exhibits higher $\Delta\mu$ (40.02 D) as compared to PMDPA ($\Delta\mu = 17.20$ D). The highly polar excited state of PMTPA is due to a higher Onsager radius (a), resulting in a higher Stokes shift in all solvents compared to PMDPA. The results suggested pronounced ICT character of PMTPA over PMDPA.

(d) Fluorescence quantum yield and lifetime:

The fluorescence quantum yields of D-A-D compounds were estimated by comparison with quinine hemisulfate monohydrate as a reference dye in water ($\Phi_f = 59\%$).¹⁰

$$\Phi_{f,x} = \Phi_{f,s} * \frac{F_x}{F_s} * \frac{f_s}{f_x} * \frac{n_x^2}{n_s^2} \quad \dots \text{ (S6)}$$

Where Φ_f is the quantum yield of the fluorophore and the subscripts x and s refer to the sample and standard, respectively. F represents integral fluorescence, n refers to the refractive index of the solvent. The absorption factor (f) at the excitation wavelength is given by Eq. S.7.

$$f = 1 - 10^{-\varepsilon(\lambda_{ex})cl} = 1 - 10^{-A(\lambda_{ex})} \quad \dots \text{ (S7)}$$

Where A is the absorbance and ε is the molar extinction coefficient ($M^{-1} \text{ cm}^{-1}$).

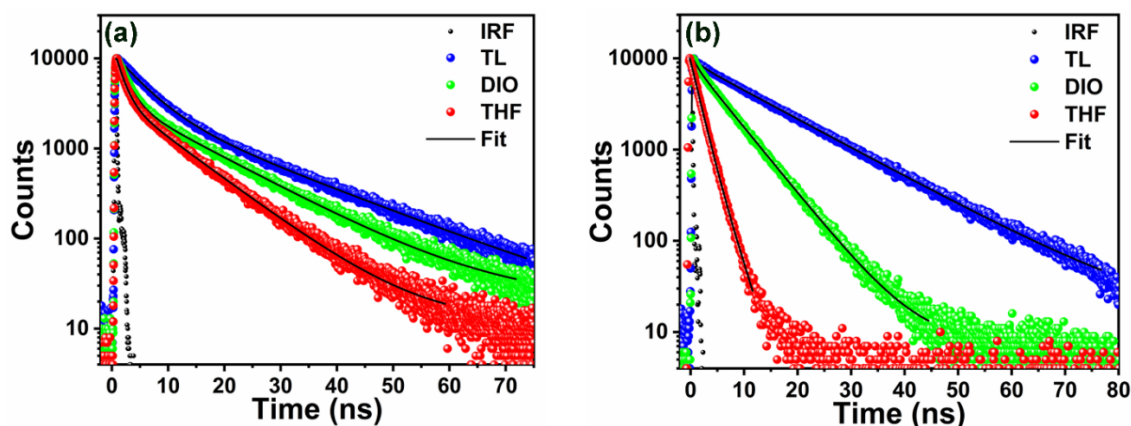


Fig. S6 Fluorescence decay profiles of (a) PMDPA ($\lambda_{\text{ex}} = 510$ nm) and (b) PMTPA ($\lambda_{\text{ex}} = 468$ nm) in the solvents of different polarities; TL: toluene, DIO: 1,4-dioxane, THF: tetrahydrofuran.

The fluorescence quantum yield of the PM-based D-A-D compounds decreases with increasing solvent polarity, as shown in Tables S3, S4. Both the compounds exhibit a biexponential fluorescence decay in different solvents at room temperature (Fig. S6, Table S3, S4). The biexponential fluorescence decay of D-A-D compounds might be due to the emission from the locally excited (LE) and the ICT state.¹

(e) Spectroscopic data tables:

Table S3 Spectroscopic data of PMDPA in various polar organic solvents; lifetime (ns) and the quality of fitting (χ^2) for the data are shown.

Solvent		Abs	FL	QY	Stokes shift	$\Delta\bar{\nu}$	Lifetime (ns) ($\lambda_{\text{ex}} = 510$ nm)				
Entry	E_N^T	λ_{abs} (nm)	λ_{em} (nm)	%	(nm)	(cm^{-1})	τ_1	α_1	τ_2	α_2	(χ^2)
Toluene	0.099	520	630	40	110	3357	3.3	1.79	20.1	98.21	1.02
Dioxane	0.164	520	675	30	155	4415	1.8	0.88	23.8	99.12	1.01
THF	0.207	521	690	15	169	4701	6.7	5.90	13.3	94.10	1.09
CHCl_3	0.259	524	720	8	196	5195	ND	ND	ND	ND	ND
DCM	0.309	522	735	7	213	5551	ND	ND	ND	ND	ND

ND: not detected

Table S4 Spectroscopic data of PMTPA in various polar organic solvents; lifetime (ns) and the quality of fitting (χ^2) for the data are shown.

Solvent		Abs	FL	QY	Stokes shift	$\Delta\bar{\nu}$	Lifetime (ns) ($\lambda_{\text{ex}} = 468$ nm)				
Entry	E_N^T	λ_{abs} (nm)	λ_{em} (nm)	%	(nm)	(cm^{-1})	τ_1	α_1	τ_2	α_2	(χ^2)
Toluene	0.099	468	603	13	138	4921	1.6	1.38	14.0	98.62	1.03
Dioxane	0.164	468	626	7	158	5393	1.1	3.20	6.1	96.80	1.04
THF	0.207	469	705	3	236	7137	5.6	7.39	1.7	92.61	1.07
CHCl_3	0.259	470	715	<0.1	245	7290	ND	ND	ND	ND	ND
DCM	0.309	470	740	<0.1	270	7763	ND	ND	ND	ND	ND

ND: not detected

V. Cyclic voltammetry

Cyclic voltammetry of ferrocene was carried out for calibration of the instrument. The half-cell potential of ferrocene-ferrocenium was found to be 0.50 V vs. Ag/AgCl. (Fig. S7). Both diphenylamine (DPA) and triphenylamine (TPA) showed an irreversible cyclic voltammogram with the half-wave potential of +1.17 and +1.13 V vs. Ag/AgCl, respectively, indicating their oxidation efficiency (Fig. S8a). On the other hand, cyclic voltammogram of the acceptor core (PM) showed the two-step single-electron reduction with half-cell potential -1.02 and -1.48 V vs. Ag/AgCl, respectively (Fig. S8b). The differential pulse voltammetry (DPV) in DCM revealed two peaks for PMDPA and a broad peak for PMTPA (Fig. S9). Table S5 showed the redox potentials of PM, PMDPA, and PMTPA in DCM. A peak at -0.87 V vs. Ag/AgCl in the negative potential window was observed in the cyclic voltammograms due to the reduction of dissolved oxygen present in the solvent (Fig. 2b), which was difficult to remove.¹¹

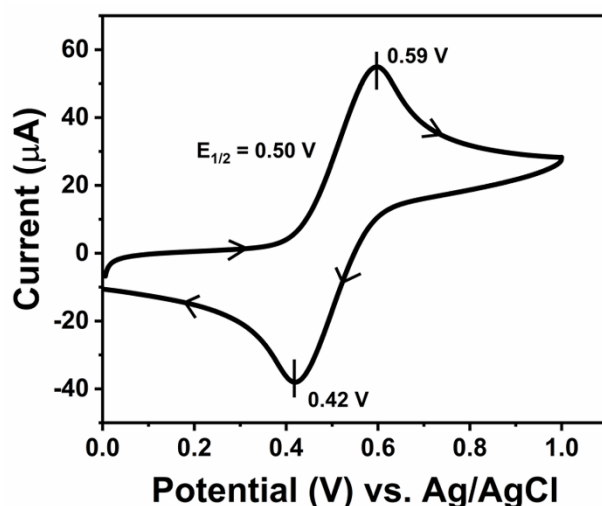


Fig. S7 Cyclic voltammogram (100 mV/s) of ferrocene (1 mM solution) in DCM using 0.1 M tetrabutylammonium hexafluorophosphate (TBAP) as supporting electrolyte and glassy carbon as the working electrode and Ag/AgCl as a reference electrode.

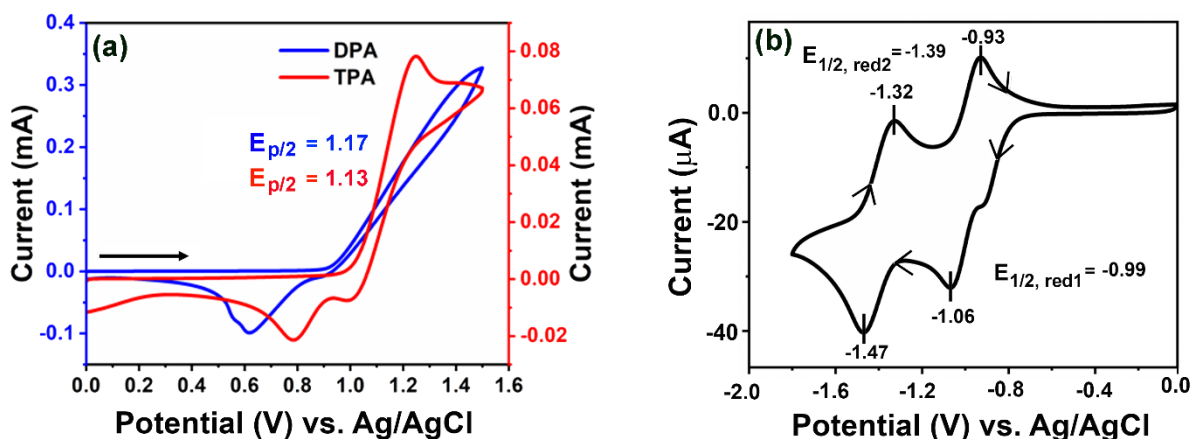


Fig. S8 Cyclic voltammogram (100 mV/s) of (a) diphenylamine (DPA) and triphenylamine (TPA), and (b) PM in DCM using 0.1 M tetrabutylammonium hexafluorophosphate (TBAP) as supporting electrolyte and glassy carbon as the working electrode and Ag/AgCl as a reference electrode.

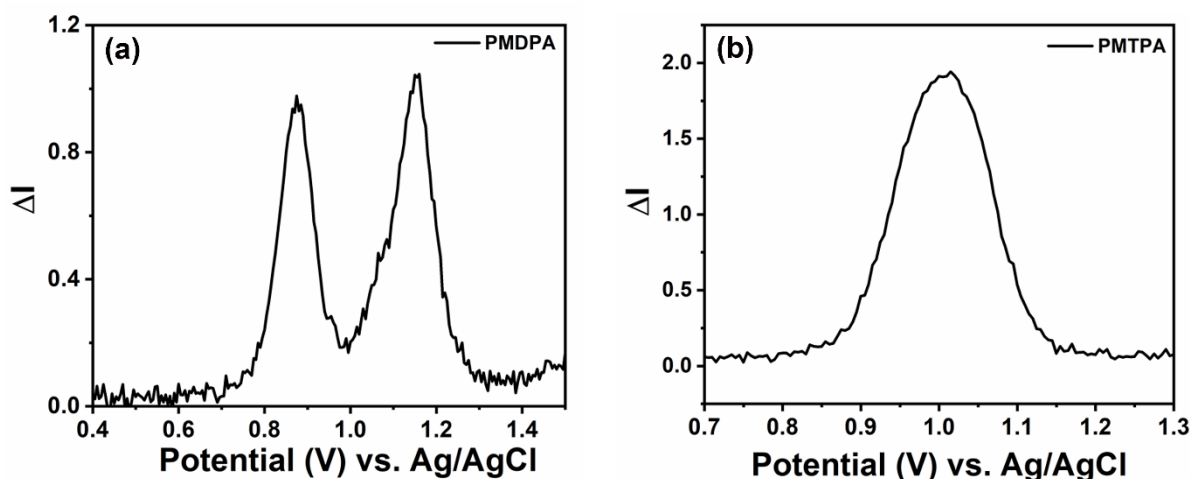


Fig. S9 Differential pulse voltammetry (DPV conditions: modulation amplitude = 2.5 mV, modulation time = 100 ms, interval time = 500 ms, step potential = 5 mV, scan rate = 0.01 mV/ms) of (a) PMDPA and (b) PMTPA in dry dichloromethane (1 mM solution) using 0.1 M tetrabutylammonium hexafluorophosphate (TBAP) as supporting electrolyte and glassy carbon as the working electrode and Ag/AgCl as a reference electrode.

Table S5 Comparative table of electrochemical data of PM, PMDPA, and PMTPA; E_{red} and E_{ox} (half-cell potentials in V) are measured in dry DCM with supporting electrolyte (0.1 M TBAP) against the reference electrode Ag/AgCl (scan rate: 100 mV/s).

System	$E_{\frac{1}{2},red1}$	$E_{\frac{1}{2},red2}$	$E_{\frac{1}{2},ox1}$	$E_{\frac{1}{2},ox2}$
PM	-0.99	-1.39	-	-
PMDPA	-1.09	-1.35	0.86	1.14
PMTPA	-1.07	-1.36	1.01	-

VI. Electrochemical stability of D-A-D compounds

The cyclic voltammetry up to the 100th cycle (Fig. 3c) and the chronoamperometry study applying switching potential of +1.3 V and 0 V vs. Ag/AgCl revealed high electrochemical stability of PMDPA (Fig. S10). The steady current density throughout the continuous cycles (time: ~ 600 s) was observed. Further, the electrochromic switching at 470 nm under the applied alternate electric potential of +1.3 V and -0.2 V vs. Ag/AgCl for multiple cycles indicated excellent electrochemical stability of PMDPA (Fig S11).

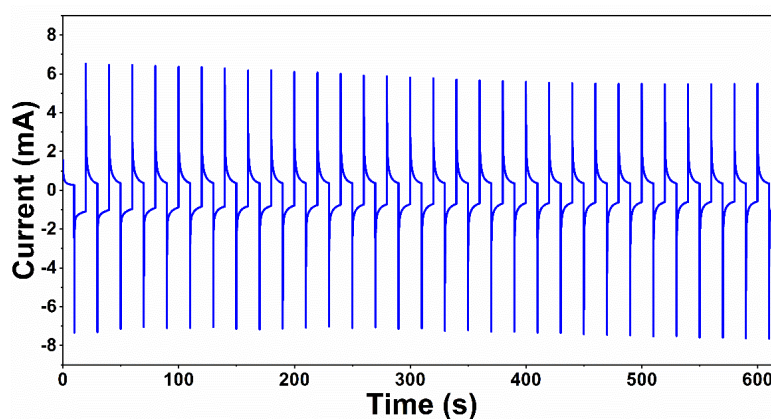


Fig. S10 Stability of the neutral and dicationic state of PMDPA in the liquid state via applied switching potential 0 and +1.3 V vs. Ag/AgCl.

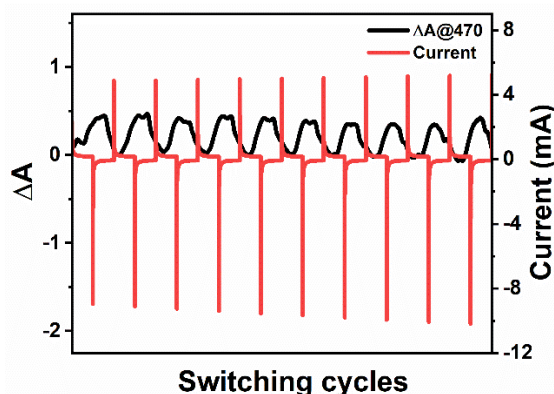


Fig. S11 Absorbance difference (ΔA , left scale) monitored at 470 nm and current (right scale) as a function of switching cycles for double potential step chronoamperometry between +1.3 V and -0.2 V vs. Ag/AgCl in DCM using 0.1 M TBAP as supporting electrolyte and Pt mesh as working electrode over 10 oxidation/reduction cycles.

On the other hand, PMTPA is electrochemically less stable, as shown by the cyclic voltammetry data (Fig. 3e), where the current intensity steadily increases with the increasing no of cycles. The observation was attributed to the weak electronic coupling between the two sp^3 hybridised nitrogen centers. As reported in the literature, a less stable radical cation led to the oligomeric product upon electrochemical oxidation of triphenylamine moiety.¹²⁻¹⁵ The FTIR and solid-state UV-Vis absorption of the electrooxidised film was carried out. The peaks

ranging from 620 to 750 cm^{-1} correspond to the C–H bending vibrations of the peripheral phenyl groups (monosubstituted benzene ring) in PMTPA (Fig. S12). The peak intensity decreased significantly for the electrooxidised product (EP-PMTPA). The noticeable increase in the intensity of the peak at 833 cm^{-1} , corresponding to the C–H bending vibrations of 1,4 disubstituted benzene ring, indicated the facile coupling reaction between the peripheral phenyl groups of PMTPA during the electrooxidation process.¹² The EP-PMTPA showed a slight red-shift on the absorption maximum in UV-Vis absorption spectra than PMTPA, indicating a more extended conjugation due to the coupling reaction (Fig. S13).

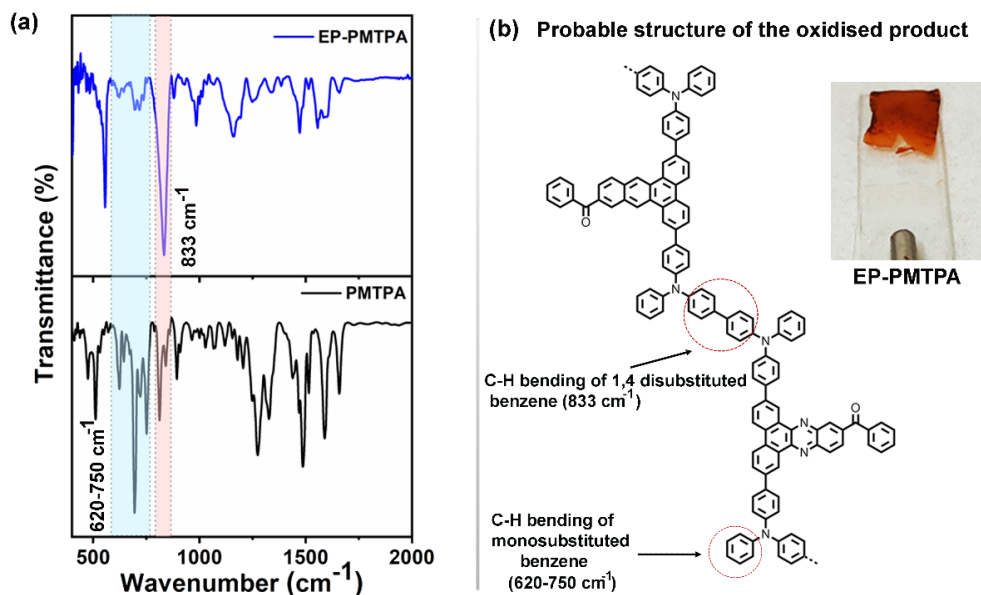


Fig. S12 (a) Fourier transform infrared (FTIR) spectra of PMTPA and electrooxidised product (EP-PMTPA). (b) Schematic depiction of the probable structure of the oxidised product; inset: digital photograph of the EP-PMTPA film on an ITO plate.

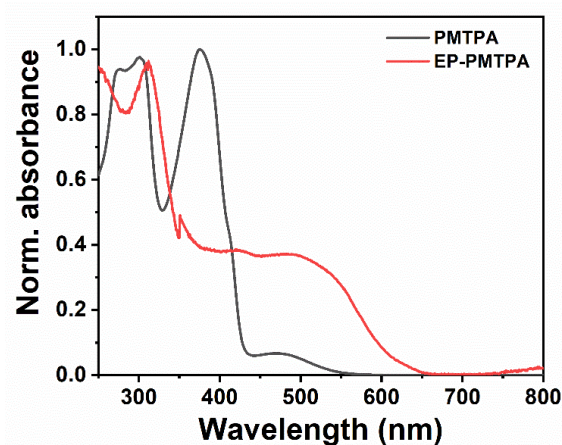


Fig. S13 Normalized UV-vis absorption spectra of PMTPA and EP-PMTPA deposited on an ITO plate.

VII. Cathodic electrochromic properties of PMDPA

Cyclic voltammetry of PMDPA in the negative potential range showed the presence of a distinct redox peak (Fig. 2b). It is due to the presence of two sp^2 hybridised nitrogen atoms in the central phenazine core. The bulk electrochemical reduction was carried at -1.3 V on PMDPA, considering its electrochemical stability (Fig. S14). The emergence of the new peaks at 450, 720, and 1020 nm attributed to the formation of radical anion species, indicating the promising scope of D-A-D based compounds for cathodically coloring material.

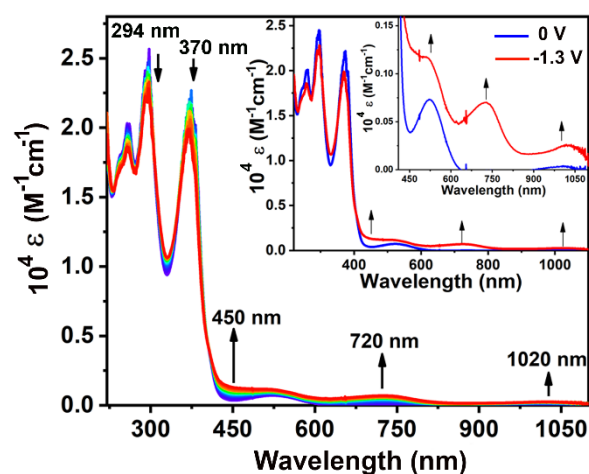


Fig. S14 Spectroelectrochemistry of PMDPA: UV-Vis-NIR absorption spectra of PMDPA upon bulk electrochemical reduction at -1.3 V vs. Ag/AgCl in DCM; inset: absorption spectra of PMDPA in DCM after applying a voltage of 0 V and -1.3 V, indicating clear emergence of new peaks at 450, 720 and 1020 nm.

VIII. Chemical oxidation of PMDPA and PMTPA by SbCl_5

(a) UV-Vis-NIR absorption:

Antimony pentachloride (SbCl_5) is a well-known chemical oxidant for organic compounds.^{16,17} Chemical oxidation of PMDPA and PMTPA was carried out by step-wise addition of SbCl_5 in DCM. The emergence of new peaks at 474, 615, 780, and 1525 nm indicated the formation of radical cation and dicationic species of PMDPA (Fig. S15a). Upon initial addition of SbCl_5 , an isosbestic point was observed at 407 nm, signifying an equilibrium between the neutral and radical cationic species. Along with that, another isosbestic point was observed at 1033 nm on further addition of SbCl_5 , indicating an equilibrium between radical cation and dicationic species. All the data were well corroborated with the results obtained through electrochemical oxidation of PMDPA (Fig. 3a, 3b). The isosbestic point was also found at 400 nm upon bulk electrooxidation at +0.95 V and +1.3 V vs. Ag/AgCl .

The sequential generation of $[\text{PMTPA}]^+$ to $[\text{PMTPA}]^{++}$ in chemical oxidation, contrary to that of the electrochemical oxidation, was possible due to the absence of any coupling reactions upon SbCl_5 addition (Fig. S15b). The isosbestic points were observed at 430, 1130 nm for PMTPA, suggesting an analogous step-by-step formation of radical cation and dicationic species like in PMDPA. The isosbestic point was also observed at 422 nm for PMTPA upon electrooxidation at +1.1 V vs. Ag/AgCl (Fig. 3d). The intensity of the IVCT band of PMTPA was less than that of PMDPA due to the weak electronic coupling in the former.¹⁸

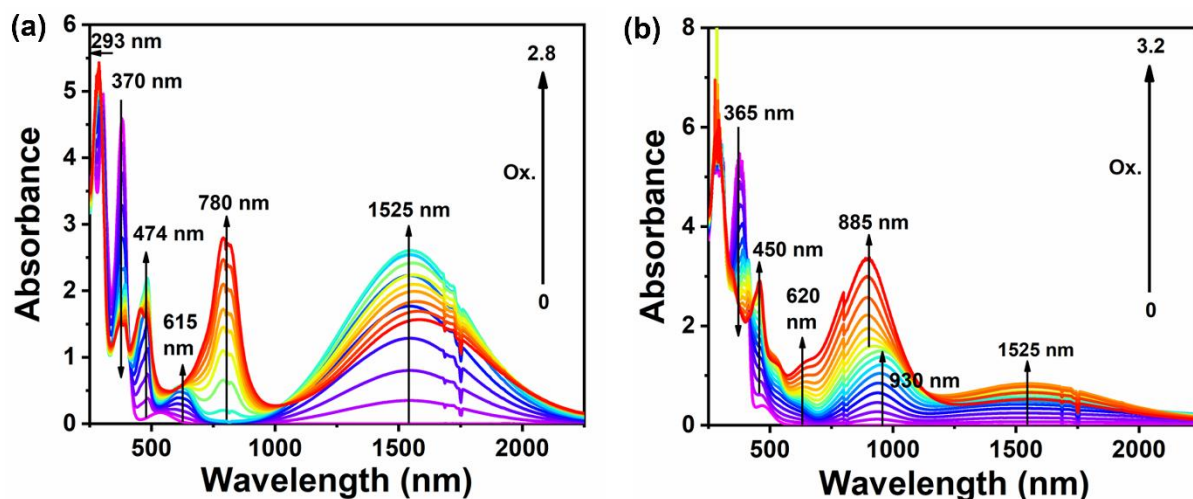


Fig. S15 UV-Vis-NIR absorption spectra of (a) PMDPA and (b) PMTPA upon oxidation by SbCl_5 in DCM as a function of Ox., where $\text{Ox.} = [\text{SbCl}_5]/[\text{PMDPA}]$, $[\text{PMDPA}] = 9 \times 10^{-5} \text{ mol L}^{-1}$ in case of (a) and $\text{Ox.} = [\text{SbCl}_5]/[\text{PMTPA}]$, $[\text{PMTPA}] = 9 \times 10^{-5} \text{ mol L}^{-1}$ in case of (b).

(b) IVCT analysis:

In order to study the intervalence charge transfer (IVCT) characteristics of the mixed-valence D-A-D compounds and to find the class to which it belongs, the full widths at half-height ($\bar{\nu}_{\frac{1}{2}[obs]}$) of the IVCT peaks were calculated from Fig. S15a and S15b and compared with the widths predicted from Hush theory (Eq. S. 8).¹⁹

$$\bar{\nu}_{\frac{1}{2}[Hush]} = \sqrt{(2310 \times \bar{\nu}_{max})} \quad \dots \quad (S8)$$

Where, $\bar{\nu}_{max}$ is the wavenumber of the absorption maximum for the IVCT peak.

In addition to that, the ratio between $\bar{\nu}_{\frac{1}{2}[high]}$ and $\bar{\nu}_{\frac{1}{2}[low]}$ for both the compounds was estimated, where $\bar{\nu}_{\frac{1}{2}[high]}$ and $\bar{\nu}_{\frac{1}{2}[low]}$ is twice the half-width on the high and low-energy side of the IVCT band. The asymmetric nature of the IVCT band was predicted via the ratio of $\bar{\nu}_{\frac{1}{2}[high]}$ and $\bar{\nu}_{\frac{1}{2}[low]}$ (Table S6). The ratio was found to be 1.5 (more asymmetric) for PMDPA, which was comparable with the typical value for a class III mixed-valence compound.¹⁸ On the other hand, for PMTPA, the ratio was found to be 1.4 (less asymmetric), suggesting PMTPA is class II mixed-valence compounds. The value of $\bar{\nu}_{\frac{1}{2}[Hush]}$ (cm^{-1}) was comparable to that of the $\bar{\nu}_{\frac{1}{2}[high]}$ (cm^{-1}) for PMTPA, and the ratio of $\bar{\nu}_{\frac{1}{2}[high]}$ and $\bar{\nu}_{\frac{1}{2}[Hush]}$ was found to be higher compared to PMDPA, again suggesting that PMTPA is a class II mixed-valence compound, whereas PMDPA is a class III according to Robin and Day classification.¹⁸⁻²³

Table S6 Experimental data obtained from the IVCT analysis of PMDPA and PMTPA radical cations in DCM upon addition of SbCl_5 .

Compd.	$\bar{\nu}_{max}$ (cm^{-1})	ϵ_{max} (M^{-1} cm^{-1})	$\bar{\nu}_{\frac{1}{2}[obs]}$ (cm^{-1})	$\bar{\nu}_{\frac{1}{2}[Hush]}$ (cm^{-1})	$\bar{\nu}_{\frac{1}{2}[high]}$ (cm^{-1})	$\bar{\nu}_{\frac{1}{2}[low]}$ (cm^{-1})	$\frac{\bar{\nu}_{\frac{1}{2}[high]}}{\bar{\nu}_{\frac{1}{2}[low]}}$	$\frac{\bar{\nu}_{\frac{1}{2}[high]}}{\bar{\nu}_{\frac{1}{2}[Hush]}}$
PMDPA	6557	43833	2581	3891	3234	2132	1.5	0.83
PMTPA	6557	14166	3304	3891	3832	2706	1.40	0.99

IX. Electron paramagnetic resonance (EPR) of D-A-D compounds

The electron paramagnetic resonance (EPR) spectra were recorded to confirm the presence of the ionic species of PMDPA and PMTPA. The chemical oxidation of PMDPA and PMTPA in DCM was carried out using SbCl_5 to identify the stable radical cations. The prominent signals for the radical cations of PMDPA and PMTPA were observed at the g values 2.013 and 2.017, respectively (Fig. S16).²⁴

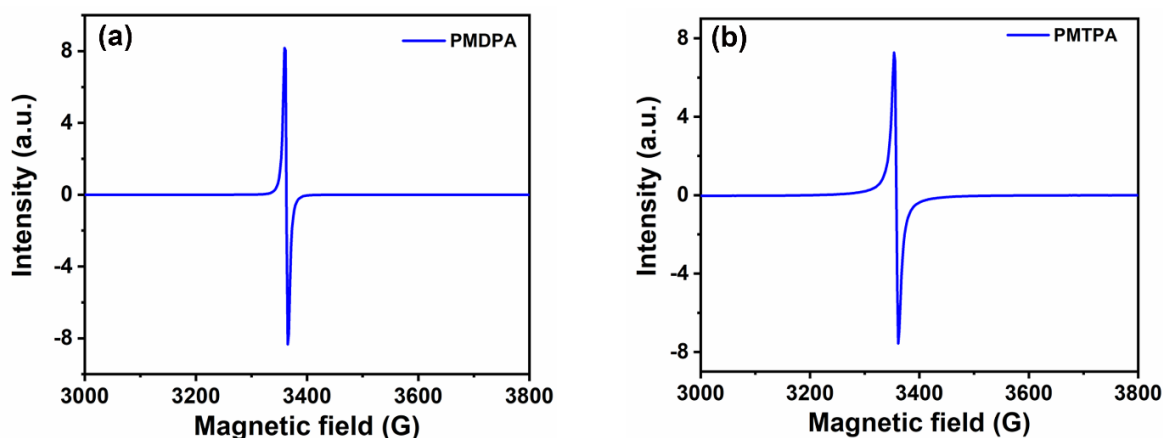


Fig. S16 Electron paramagnetic resonance (EPR) spectra of radicals formed via the chemical oxidation of (a) PMDPA and (b) PMTPA in DCM (1 mM) by SbCl_5 .

X. Electrofluorochromism of PMDPA and PMTPA

Electrofluorochromism experiment of PMDPA was carried out in tetrahydrofuran (THF), considering its high quantum yield in THF. A decrease in the emission intensity at 690 nm was observed upon bulk electrochemical oxidation at +0.95 V vs. Ag/AgCl (Fig. S17a). Excitation spectra monitored at $\lambda_{\text{em}} = 690$ nm suggested the conversion of emissive neutral PMDPA to its non-emissive radical cationic species (Fig. S17b).

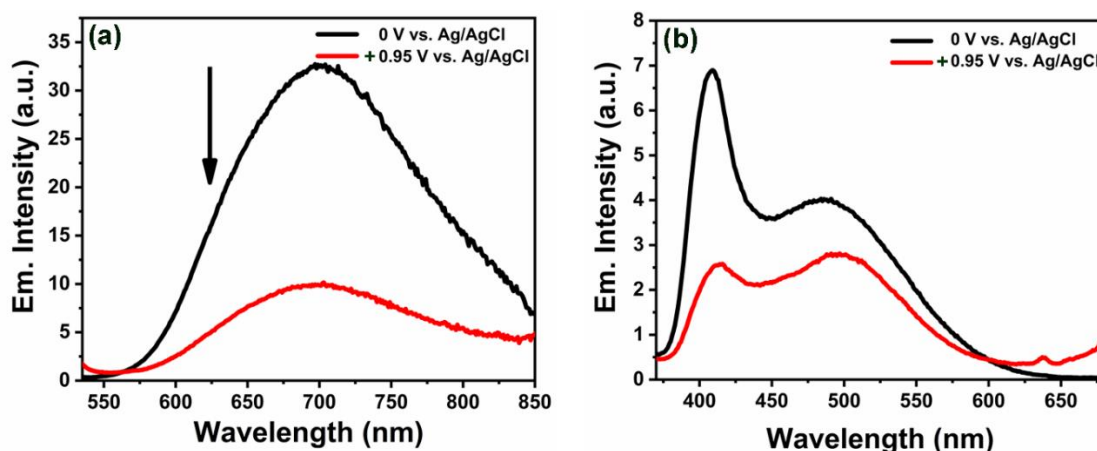


Fig. S17 (a) Emission ($\lambda_{\text{ex}} = 520$ nm) and (b) excitation spectra ($\lambda_{\text{em}} = 690$ nm) of PMDPA in 0.1 M TBAP by applying constant potential of +0.95 V vs. Ag/AgCl in THF.

Excitation spectra of PMDPA at 735 nm showed a decrease in the intensity with the addition of SbCl_5 (Fig. S18), indicating the conversion of emissive neutral species to non-emissive radical cation and dicationic species of PMDPA upon chemical oxidation.

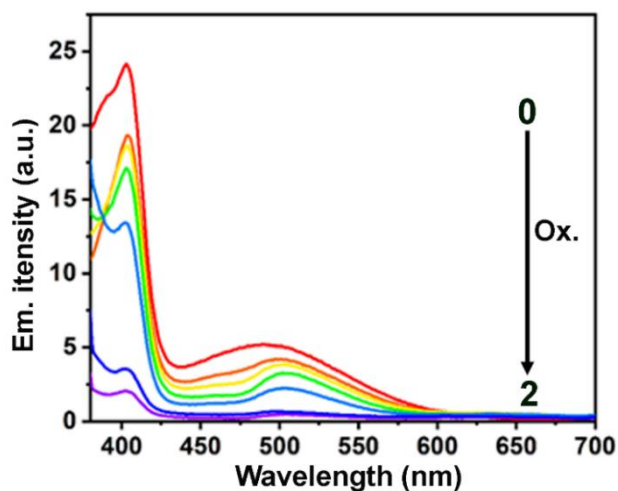


Fig. S18 Excitation spectra ($\lambda_{\text{em}} = 735 \text{ nm}$) of PMDPA upon oxidation by SbCl_5 in DCM as a function of Ox., where $\text{Ox.} = [\text{SbCl}_5]/[\text{PMDPA}]$, $[\text{PMDPA}] = 9 \times 10^{-5} \text{ mol L}^{-1}$.

A double potential step chronoamperometry in DCM was carried out at various switching potentials ranging from +1.5/-0.2 V to +0.7/-0.2 V vs. Ag/AgCl, indicating electro-switchable fluorescence (Fig. S19).

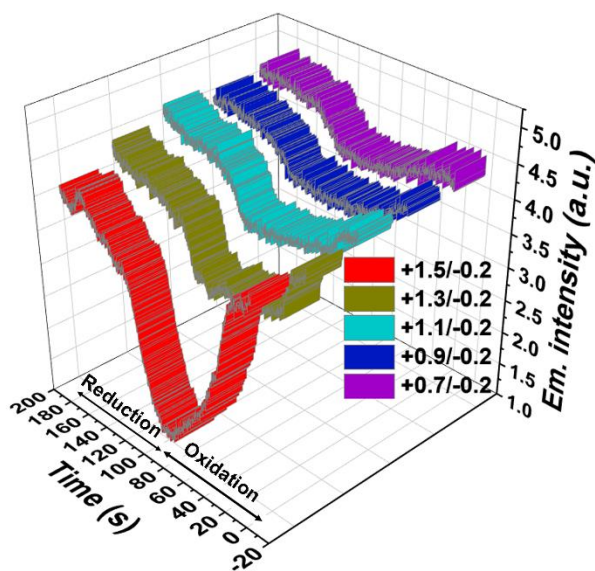


Fig. S19 3D plots of emission intensity of PMDPA vs. time for double potential step chronoamperometry at various switching potentials from +1.5/-0.2 V to +0.7/-0.2 V vs. Ag/AgCl in DCM using 0.1 M TBAP as supporting electrolyte and Pt mesh as working electrode ($\lambda_{\text{ex}} = 525 \text{ nm}$, $\lambda_{\text{em}} = 735 \text{ nm}$).

The fluorescence was found to be reversible upon repeated switching potential at +0.95 V and -0.2 V vs. Ag/AgCl (Fig. S20).

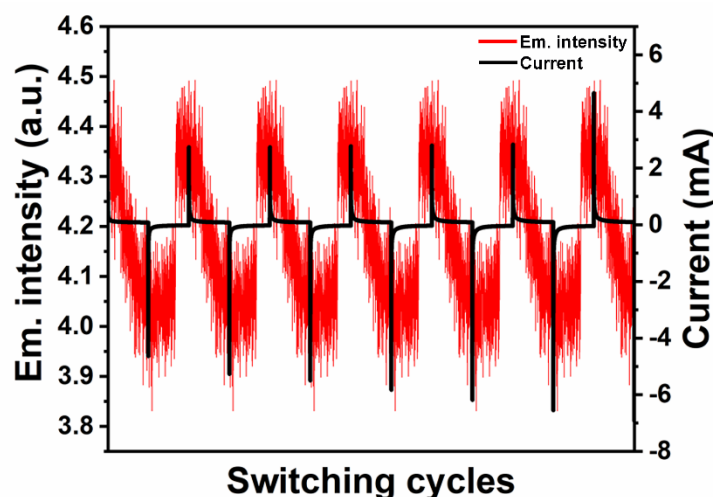


Fig. S20 Emission intensity (left scale) and current (right scale) as a function of switching cycles for double potential step chronoamperometry between +0.95 V and -0.2 V vs. Ag/AgCl in DCM using 0.1 M TBAP as supporting electrolyte and Pt mesh as working electrode ($\lambda_{\text{ex}} = 520 \text{ nm}$, $\lambda_{\text{em}} = 735 \text{ nm}$).

The electrofluorochromism experiment was carried out for PMTPA at various switching potentials ranging from +1.5/-0.2 V to +0.7/-0.2 V under identical conditions as that of PMDPA. The electrofluorochromism behaviour of PMTPA is not reversible, as seen from Fig. S21, due to the destructive side reaction after electrochemical oxidation.

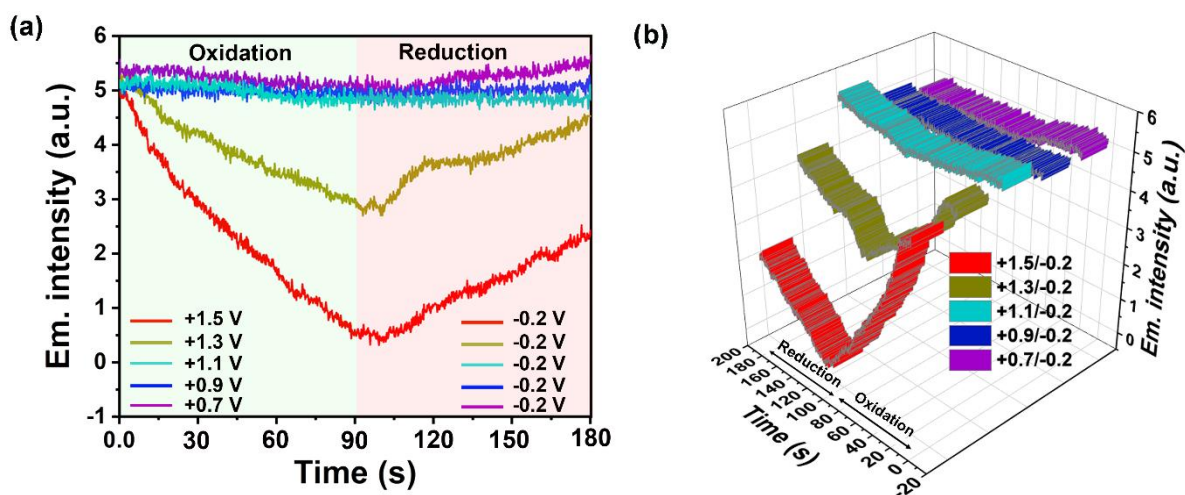


Fig. S21 (a) 2D and (b) 3D plots of emission intensity of PMTPA vs. time for double potential step chronoamperometry at various switching potentials from +1.5/-0.2 V to +0.7/-0.2 V vs. Ag/AgCl in DCM using 0.1 M TBAP as supporting electrolyte and Pt mesh as working electrode ($\lambda_{\text{ex}} = 465 \text{ nm}$, $\lambda_{\text{em}} = 740 \text{ nm}$).

XI. Computational investigations

The ground state geometries of PMDPA and PMTPA and their ionic species were optimized by the density functional theory (DFT) using CAM-B3LYP functional and 6-31G(d, p) basis set in Gaussian 09 program package. The polarizable continuum model (PCM) was employed for all the calculations using the dielectric constant of DCM. GaussView 5.0 was used to analyse the computational data. DFT calculations using unrestricted spin configuration produce the SOMO of the radical cations (Fig. S22). SOMO of $[PMDPA]^{+\bullet}$ show the equal distribution of the electron density in the donor units due to the strong electronic coupling between the amine centers. On the other hand, unequal distribution of the electron density was observed in the SOMO of $[PMTPA]^{+\bullet}$ due to the weak electronic coupling between the amine centers.

The time-dependent density functional theory (TDDFT) calculations were carried out to obtain the electronic transitions of neutral as well as ionic species of PMDPA and PMTPA, respectively (Fig. S23, S24, S25). The same hybrid functional and basis set were used in Gaussian 09 program package for the excited state calculations. For radical cation and dication, specific charges and multiplicity were added. The experimental lower energy absorption bands at 520 and 465 nm of PMDPA and PMTPA at the neutral state, respectively, were attributed to the transition between frontier molecular orbitals (HOMO to LUMO, Fig. S23, S24). At the same time, the higher energy peaks at 370 nm (PMDPA) and 365 nm (PMTPA) were referred to as the transition from HOMO to LUMO+3 (Fig. S23) and HOMO to LUMO+2 (Fig. S24), respectively. HOMO localized over the donor moieties and the phenanthrene spacer, whereas LUMO, LUMO+3 (PMDPA), and LUMO+2 (PMTPA) were mostly located on the PM acceptor core (Fig. S23, S24).

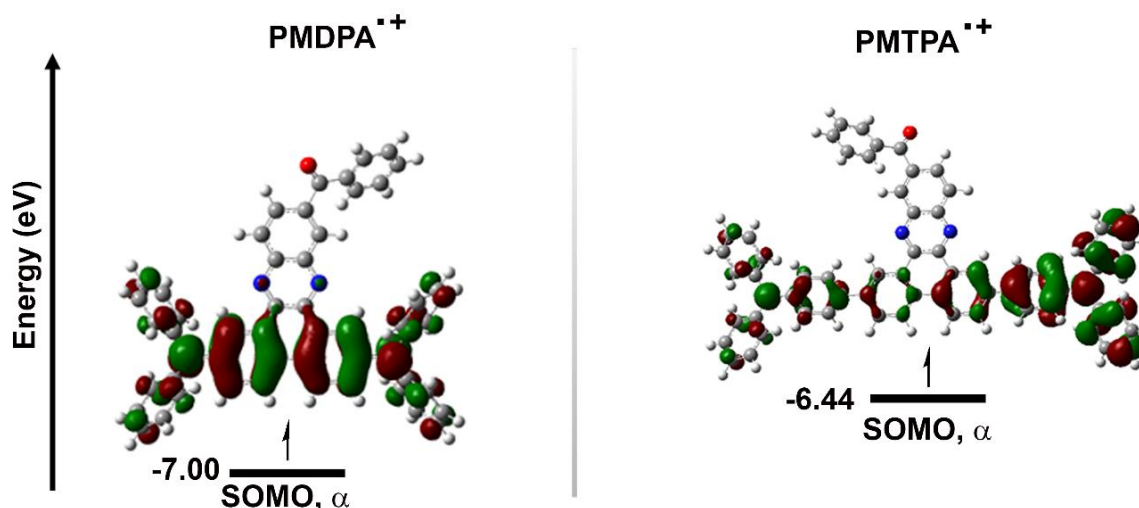


Fig. S22 Singly occupied molecular orbitals (SOMO) of $[PMDPA]^{+\bullet}$ and $[PMTPA]^{+\bullet}$ calculated using CAM-B3LYP function and 6-31G(d,p) basis set.

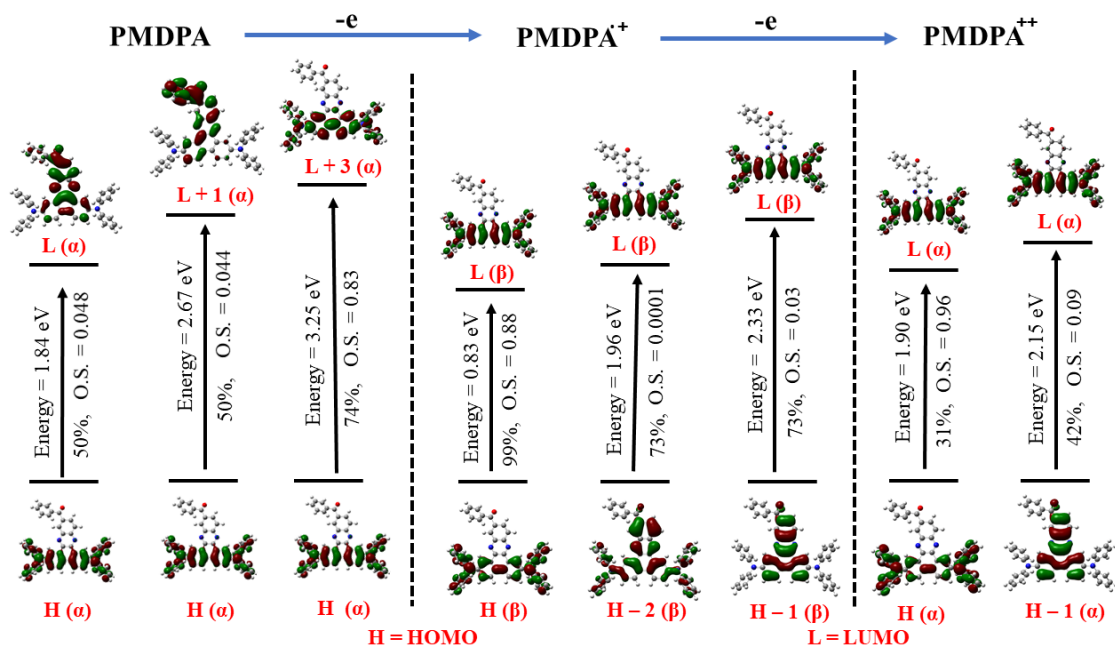


Fig. S23 TDDFT calculated most probable electronic transitions of *PMDPA*, [*PMDPA*]⁺, [*PMDPA*]⁺⁺. The transition energy, transition probability (%), and oscillator strength (O.S.) for each transition are shown.

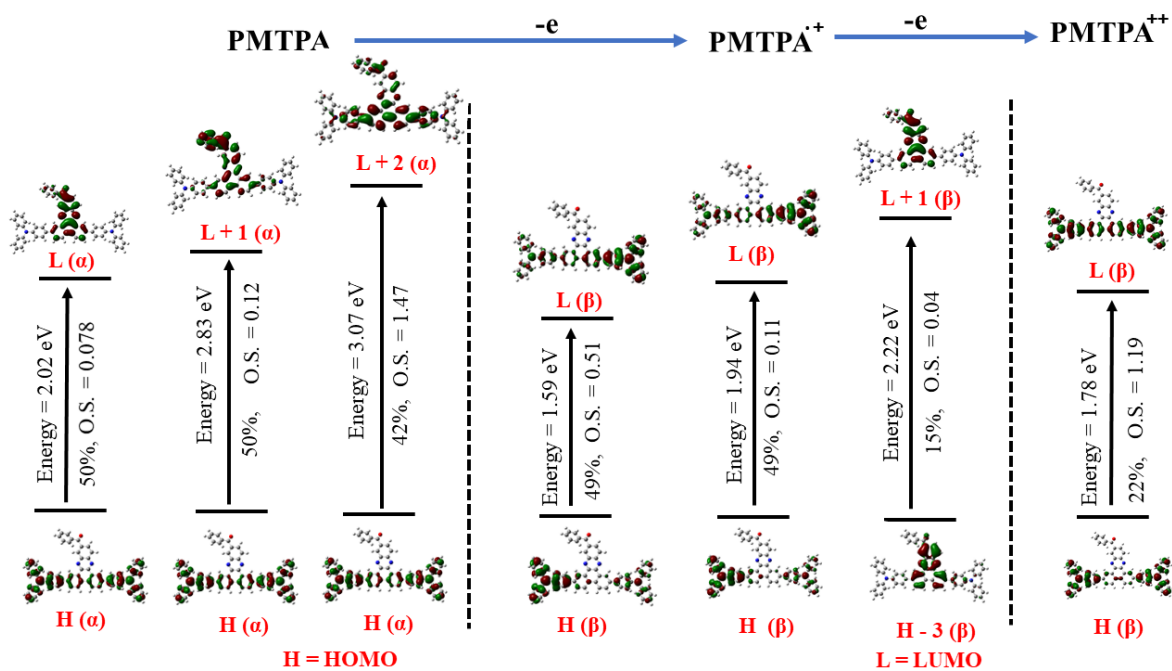


Fig. S24 TDDFT calculated most probable electronic transitions of *PMTPA*, [*PMTPA*]⁺, [*PMTPA*]⁺⁺. The transition energy, transition probability (%), and oscillator strength (O.S.) for each transition are shown.

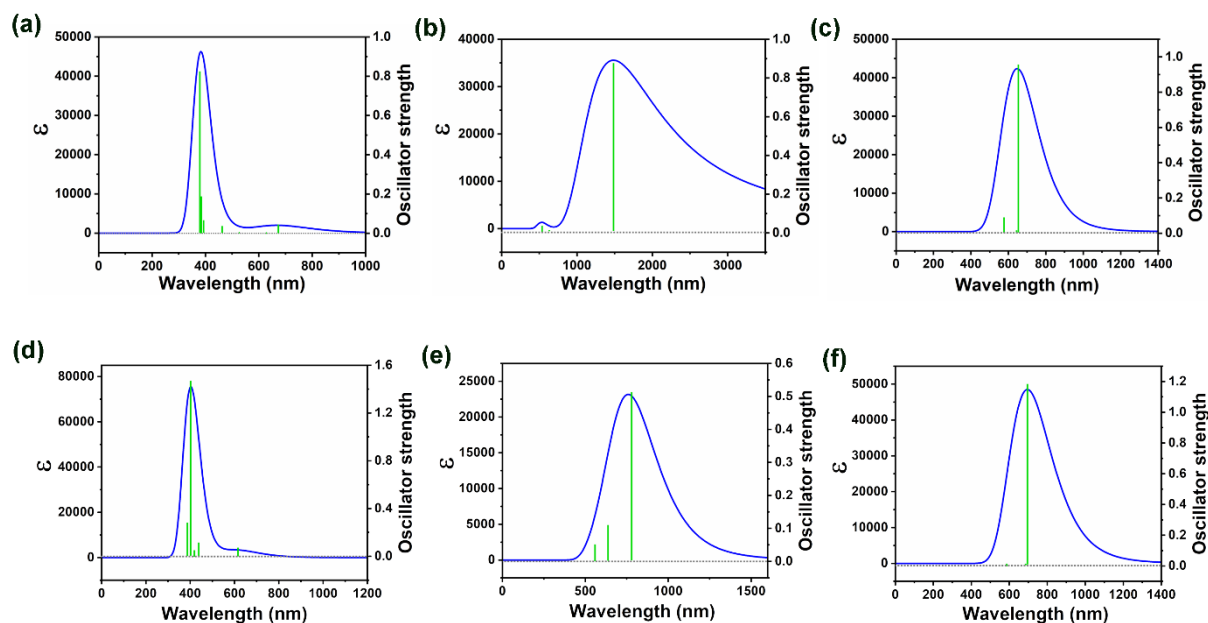


Fig. S25 TDDFT computed electronic absorption spectra of (a) *PMDPA*, (b) $[PMDPA]^{\bullet+}$, (c) $[PMDPA]^{\bullet\bullet+}$, (d) *PMTPA*, (e) $[PMTPA]^{\bullet+}$, and (f) $[PMTPA]^{\bullet\bullet+}$.

The computed spin densities of radical cationic species ($[PMDPA]^{\bullet+}$ and $[PMTPA]^{\bullet+}$) were obtained using long-range corrected functional (CAM-B3LYP) and 6-31G(d,p) basis set (Fig. 3f, S26). The polarizable continuum model (PCM) was employed for all the calculations using the dielectric constant of DCM.²⁵

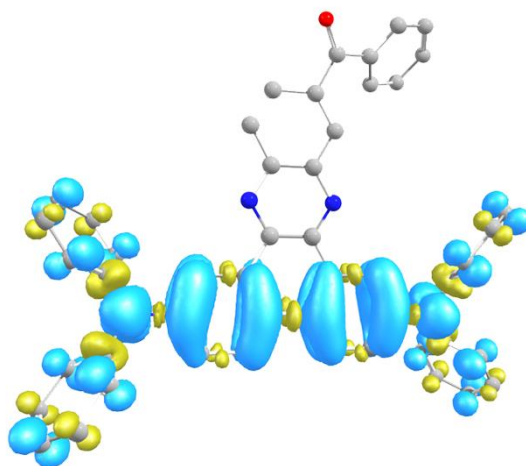


Fig. S26 DFT computed (CAM-B3LYP function and 6-31G(d,p) basis set) spin density distribution of $[PMDPA]^{\bullet+}$, isosurface value = 0.001.

XII. EC-EFC switching of the PMDPA thin film

As a proof of concept, electrochromic-electrofluorochromic (EC-EFC) switching and their stability was shown for PMDPA in the solid state by fabricating thin film on indium tin oxide (ITO) coated glass substrate (Fig. S27, S28). The color change from light pink to dark green was observed upon the applied potential of +0.95 V and subsequently to greenish-brown upon the applied potential of +1.3 V vs. Ag/AgCl (Fig. S27). The switching of fluorescence (on/off) was also observed at the applied electric potential of +1.3 V vs. Ag/AgCl under a 365 nm UV lamp due to the nonradiative deactivation after photoexcitation (Fig. S28). However, the relatively lower cyclic stability of PMDPA-PMMA thin film compared to the solution was due to the presence of a rigid matrix (PMMA), which might hinder the easy diffusion of the electrolyte ions required for charge neutrality during repetitive potential scans (Fig. S29a).²⁶ On the other hand, PMTPA-embedded PMMA thin film showed irreversible cyclic voltammograms with an increase in current intensity with the increasing number of cycles indicating electrochemical instability similar to that observed in the solution state (Fig. 3e, S29b).

The working electrode was fabricated by spin coating a viscous solution of PMDPA and poly(methyl methacrylate) (PMMA), a thermoplastic polymer in toluene on the ITO plate.²⁷ The EC-EFC measurements were carried out in a three-electrode electrochemical cell containing 0.1 M TBAP in acetonitrile-water (1:1, V/V) using Pt wire and Ag/AgCl as counter and reference electrode, respectively.

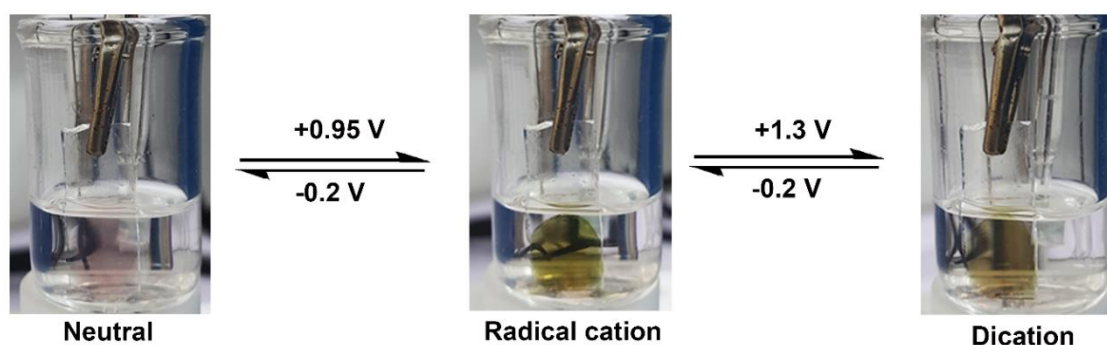


Fig. S27 Digital photographs of electrochromic switching depicting the color change from light pink to dark green and greenish-brown upon applied potentials of +0.95/-0.2 V and +1.3/-0.2 V vs. Ag/AgCl, respectively. The electrochromic switching was demonstrated in an electrochemical cell containing 0.1 M TBAP in acetonitrile-water (1:1, V/V) using PMDPA-PMMA coated ITO, Pt wire, and Ag/AgCl as a working electrode, a counter electrode, and the reference electrode, respectively.

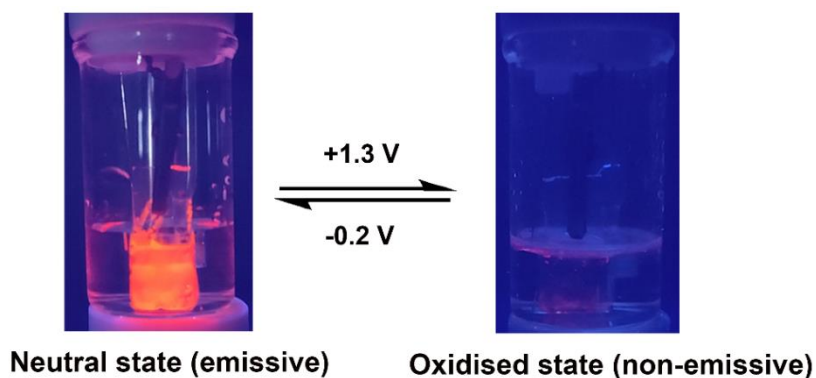


Fig. S28 Digital photographs of electrofluorochromic switching under 365 nm UV lamp depicting the fluorescence switching (on/off) upon applied potentials of +1.3 and -0.2 V vs. Ag/AgCl; fluorescence switching was shown in an electrochemical cell containing 0.1 M TBAP in acetonitrile-water (1:1, V/V) using PMDPA-PMMA coated ITO, Pt wire, and Ag/AgCl as a working electrode, a counter electrode, and a reference electrode, respectively.

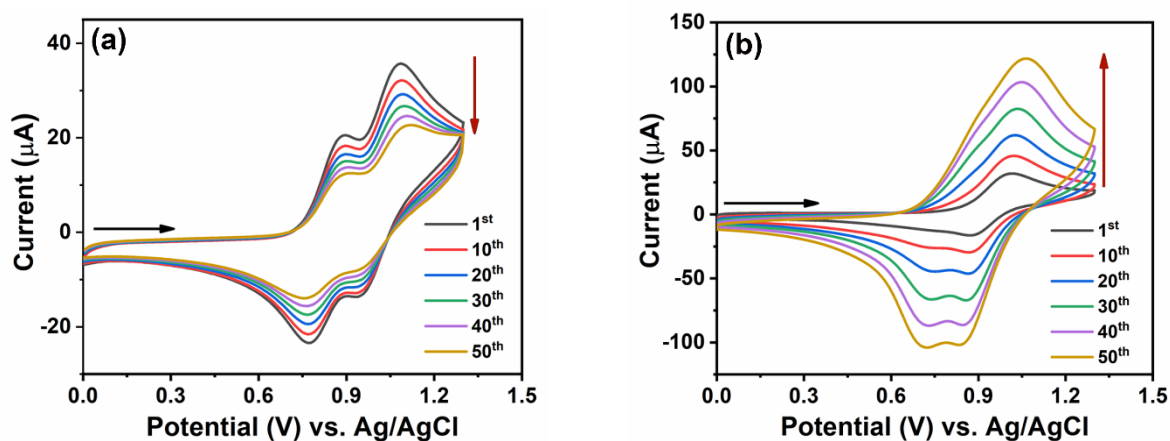


Fig. S29 Cyclic voltammograms (1st, 10th, 20th, 30th, 40th and 50th cycles) of (a) PMDPA and (b) PMTPA thin film measured in three-electrode cells containing 0.1 M TBAP in acetonitrile-water (1:1, V/V) at a scan rate 100 mV/s, using PMDPA/PMTPA-PMMA coated indium tin oxide (ITO), Pt wire and Ag/AgCl as working, counter and reference electrode, respectively. The black arrows indicate the direction of the initial scan, and the red arrows indicate the increase/decrease of current intensity.

XIII. Characterization: ^1H and ^{13}C NMR, Mass Spectra

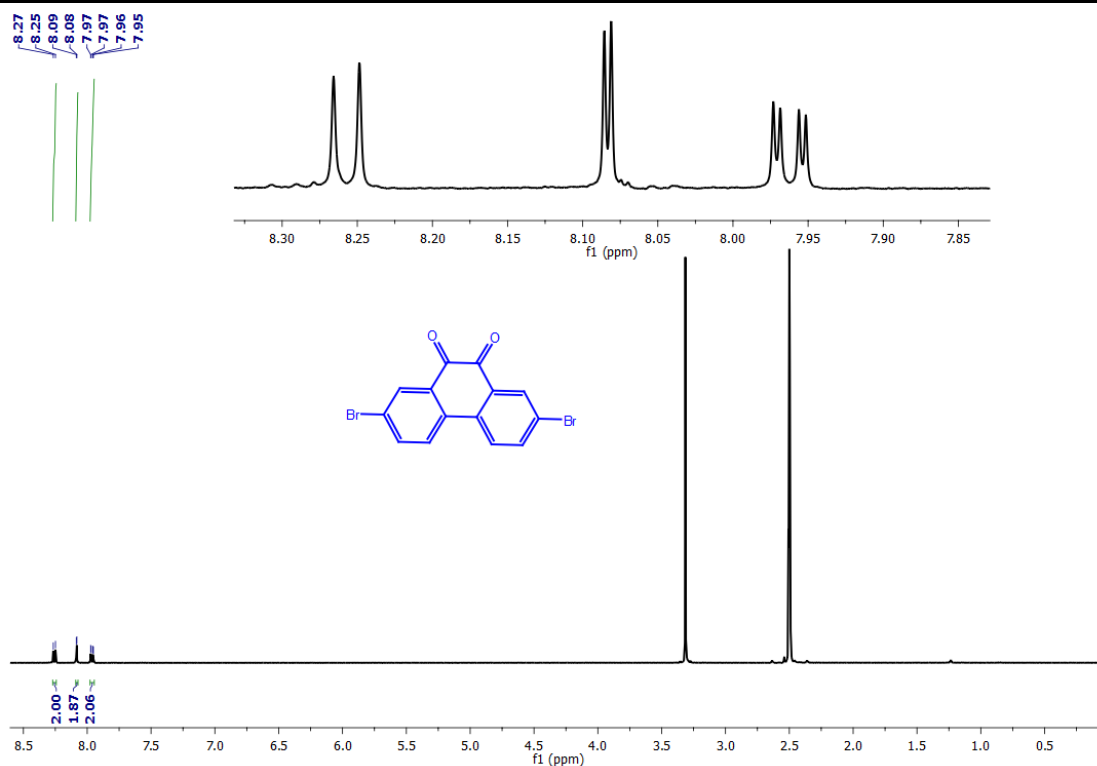


Fig. S30 ^1H NMR spectrum of 2,7-dibromophenanthrene-9,10-quinone (1) in DMSO- d_6 .

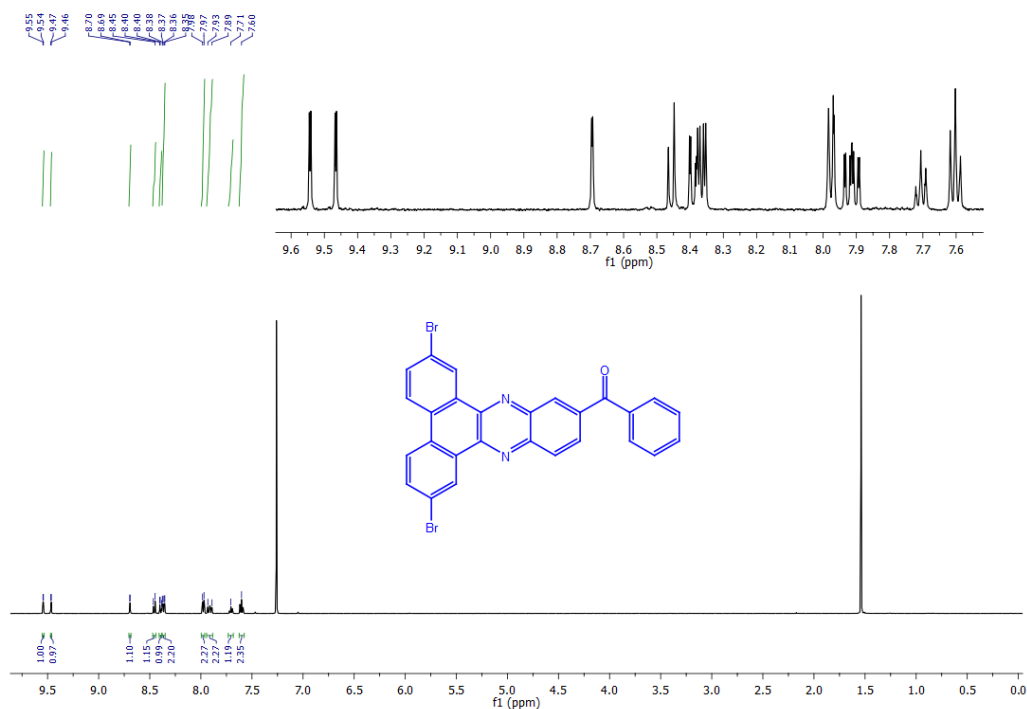


Fig. S31 ^1H NMR spectrum of 2,7-dibromodibenzo[*a,c*]phenazin-11-yl(phenyl)methanone (2) in CDCl_3 .

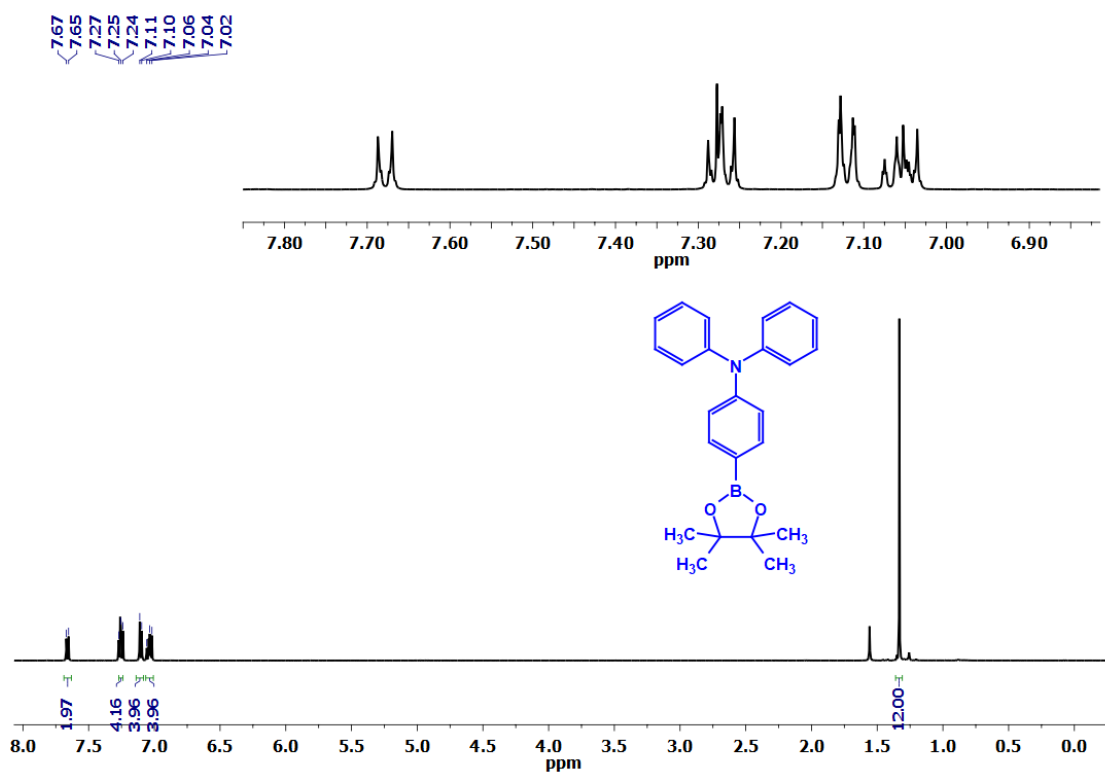


Fig. S32 ¹H NMR spectrum of *N,N*-diphenyl-4-(4,4,5,5-tetramethyl-1,3,2-dioxaborolan-2-yl)aniline (**3**) in CDCl₃.

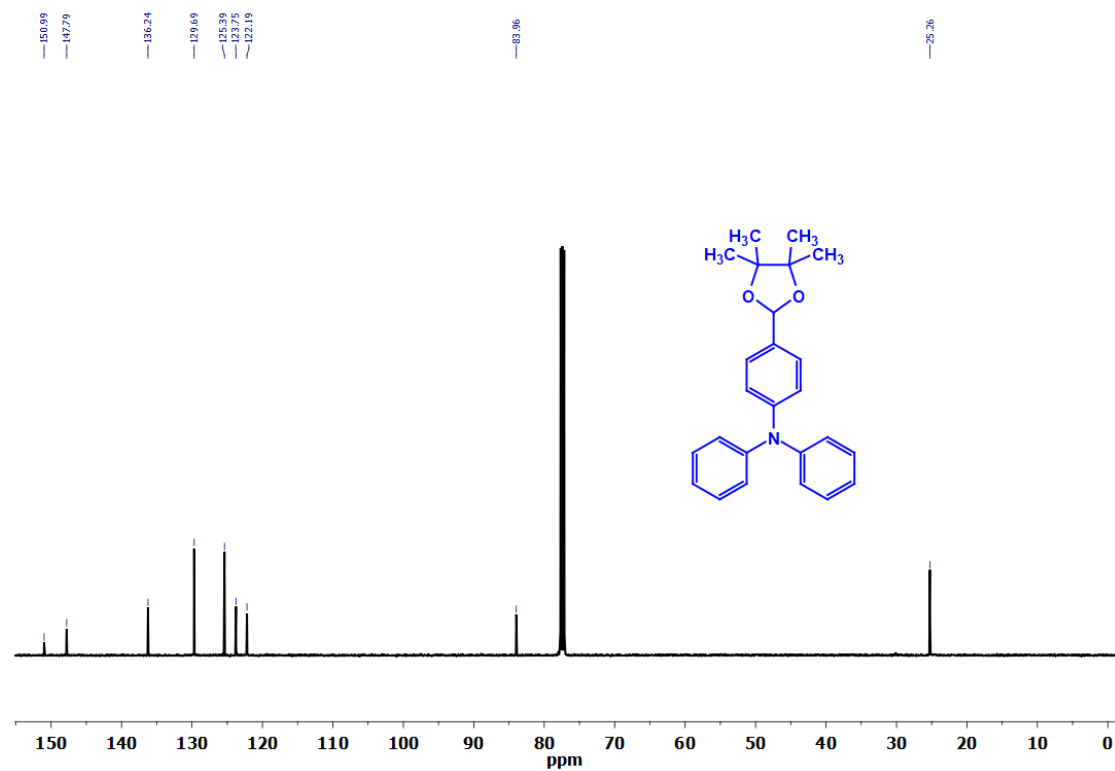


Fig. S33 ¹³C NMR spectrum of *N,N*-diphenyl-4-(4,4,5,5-tetramethyl-1,3,2-dioxaborolan-2-yl)aniline (**3**) in CDCl₃.

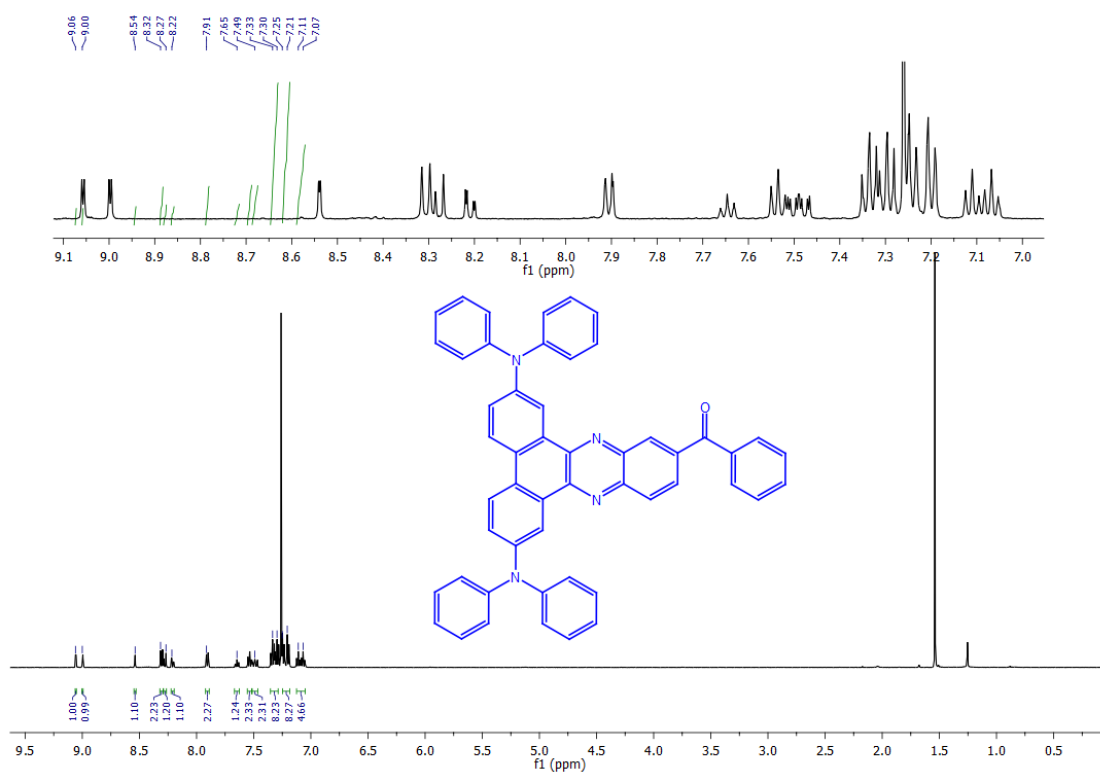


Fig. S34 ¹H NMR spectrum of PMDPA in CDCl₃.

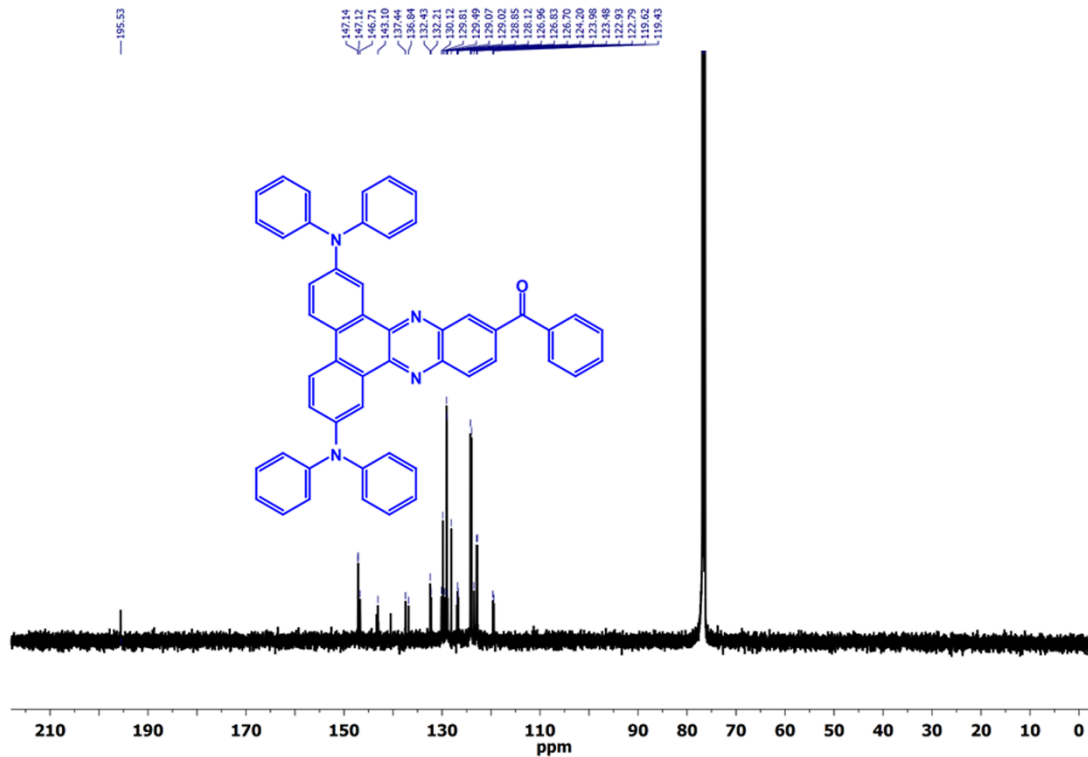


Fig. S35 ¹³C NMR spectrum of PMDPA in CDCl₃.

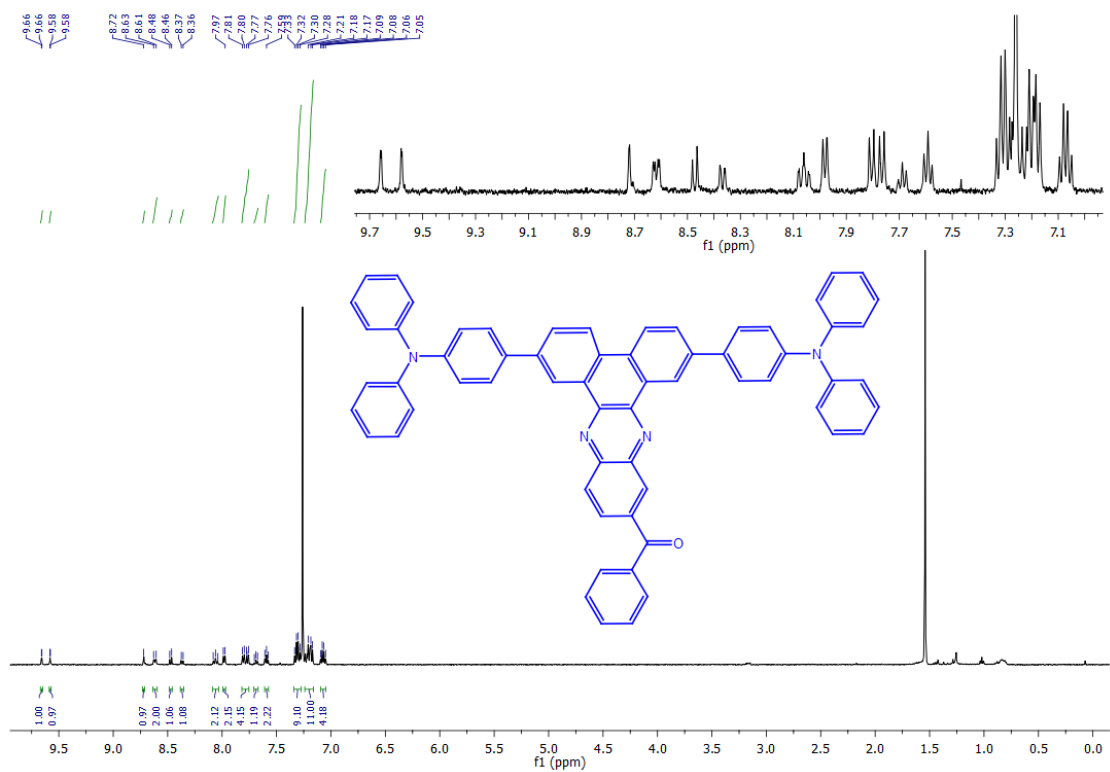


Fig. S36 ¹H NMR spectrum of PMTPA in CDCl₃.

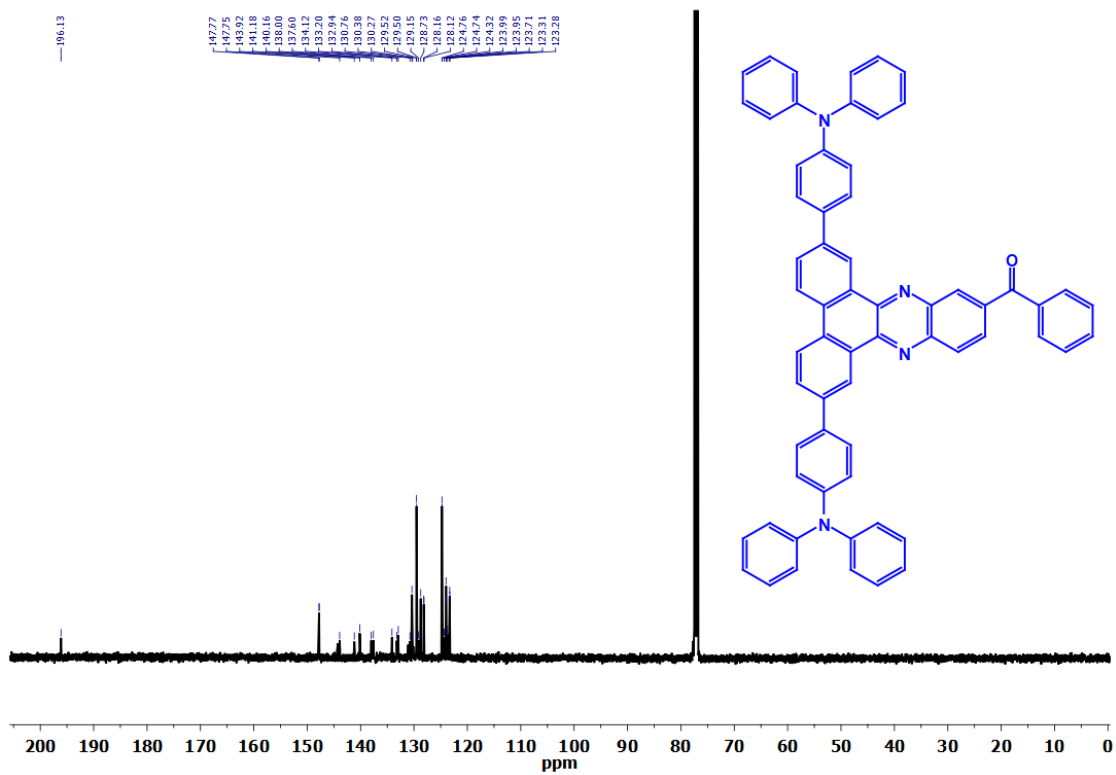


Fig. S37 ¹³C NMR spectrum of PMTPA in CDCl₃.

Display Report

Analysis Info

Analysis Name D:\Data\NEW USER DATA 2017\2018\01 March-2018\Dr.A.Patra-AP-KS-DPA.d
Method tune_wide_APCI_23.06.m
Sample Name AP-KS-DPA
Comment

Acquisition Date 3/1/2018 3:43:53 PM
Operator RUCHI
Instrument micrOTOF-Q II 10330

Acquisition Parameter

Source Type	APCI	Ion Polarity	Positive	Set Nebulizer	2.5 Bar
Focus	Not active	Set Capillary	4000 V	Set Dry Heater	200 °C
Scan Begin	50 m/z	Set End Plate Offset	-500 V	Set Dry Gas	4.0 l/min
Scan End	3000 m/z	Set Collision Cell RF	600.0 Vpp	Set Divert Valve	Waste

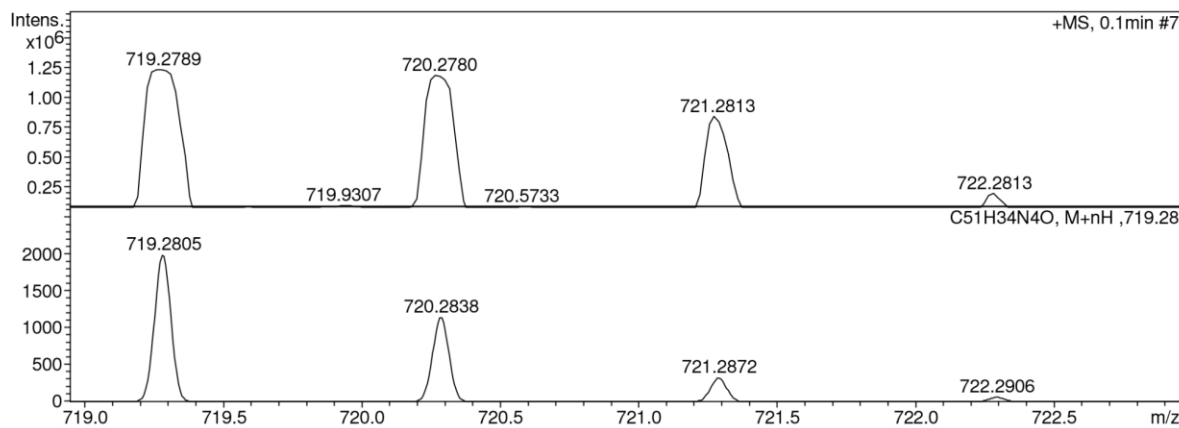
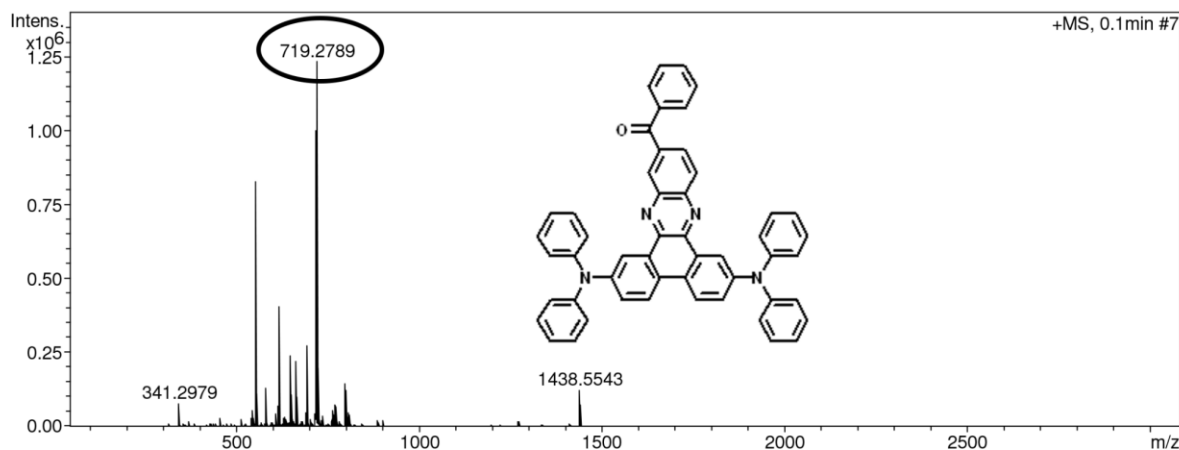
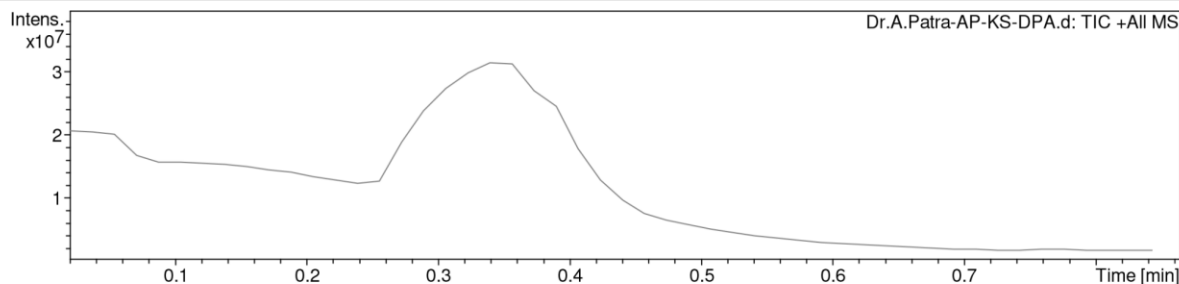


Fig. S38 HRMS (APCI) mass spectrum of PMDPA.

Display Report

Analysis Info

Analysis Name D:\Data\NEW USER DATA 2017\2018\08 march-2018\Dr.A.Patra-AP-BPM-TPA.d
Method tune_wide_APCI_23.06.m
Sample Name AP-BPM-TPA
Comment

Acquisition Date 3/8/2018 2:38:31 PM
Operator RUCHI
Instrument micrOTOF-Q II 10330

Acquisition Parameter

Source Type	APCI	Ion Polarity	Positive	Set Nebulizer	2.5 Bar
Focus	Not active	Set Capillary	4000 V	Set Dry Heater	200 °C
Scan Begin	50 m/z	Set End Plate Offset	-500 V	Set Dry Gas	4.0 l/min
Scan End	3000 m/z	Set Collision Cell RF	600.0 Vpp	Set Divert Valve	Waste

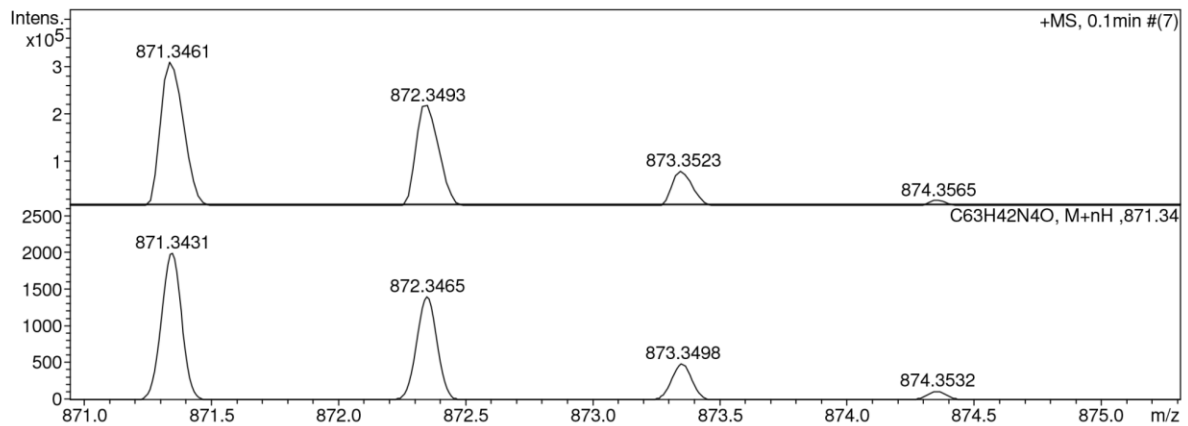
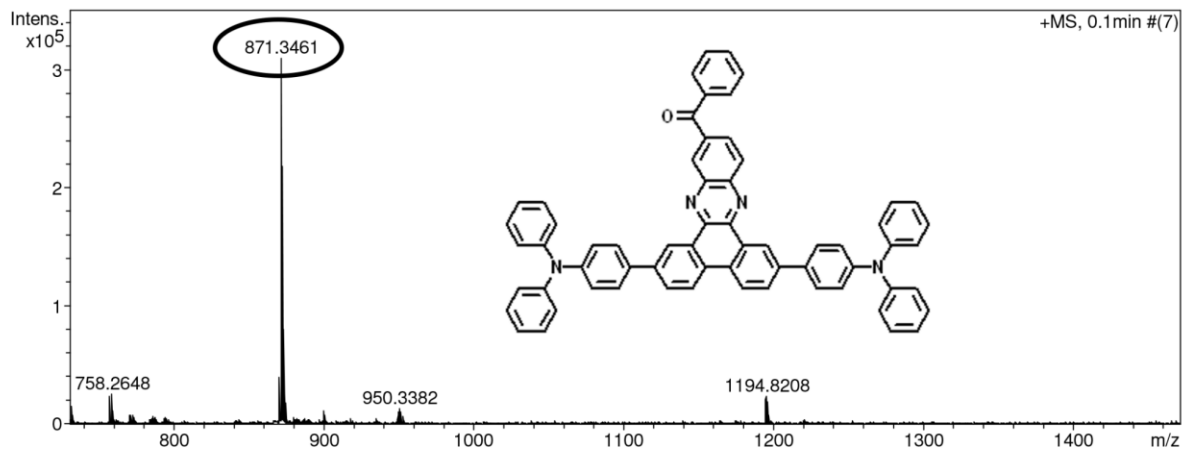
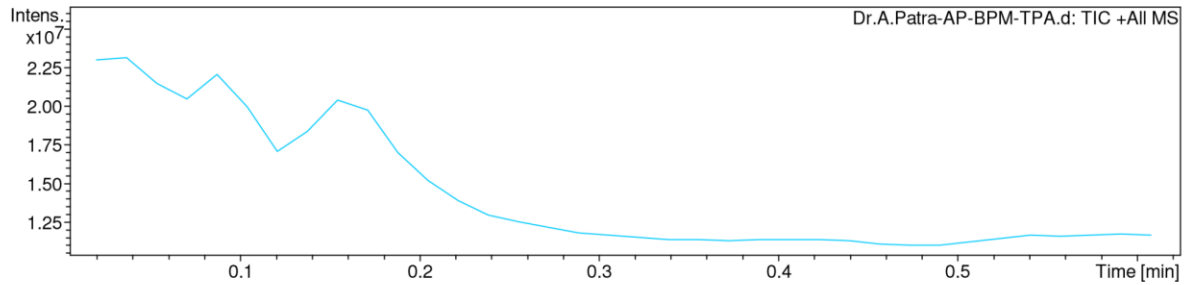


Fig. S39 HRMS (APCI) mass spectrum of PMTPA.

XIV. Reference

1. B. Sk, S. Sharma, A. James, S. Kundu and A. Patra, *J. Mater. Chem. C*, 2020, **8**, 12943.
2. P. M. Beaujuge, C. M. Amb and J. R. Reynolds, *Acc. Chem. Res.*, 2010, **43**, 1396.
3. N. Yan, W. Zhang, G. Li, S. Zhang, X. Yang, K. Zhou, D. Pei, Z. Zhao and G. He, *Mater. Chem. Front.*, 2021, **5**, 4128.
4. B. Sk, S. Khodia and A. Patra, *Chem. Commun.*, 2018, **54**, 1786.
5. D. N. Kanekar, S. Chacko and R. M. Kamble, *New J. Chem.*, 2020, **44**, 3278.
6. C. Wu, Z. Wu, B. Wang, X. Li, N. Zhao, J. Hu, D. Ma and Q. Wang, *ACS Appl. Mater. Interfaces*, 2017, **9**, 32946.
7. J. R. Lakowicz, *Principles of fluorescence spectroscopy*, Springer, New York, 2006.
8. S. Mukherjee, A. Chattopadhyay, A. Samanta and T. Soujanya, *J. Phys. Chem.*, 1994, **98**, 2809.
9. C. Reichardt, *Chem. Rev.*, 1994, **94**, 2319.
10. K. Rurack and M. Spieles, *Anal. Chem.*, 2011, **83**, 1232.
11. T. Ohsaka, M. Tsushima and K. Tokuda, *Bioelectrochem. Bioenerg.*, 1993, **31**, 289.
12. J. Sun and Z. Liang, *ACS Appl. Mater. Interfaces*, 2016, **8**, 18301.
13. R. R. Nelson and R. N. Adams, *J. Am. Chem. Soc.*, 1968, **90**, 3925.
14. H. Ma, F. Li, P. Li, H. Wang, M. Zhang, G. Zhang, M. Baumgarten and K. Müllen, *Adv. Funct. Mater.*, 2016, **26**, 2025.
15. S. Nad and S. Malik, *ChemElectroChem*, 2021, **7**, 4144.
16. R. Rathore, C. L. Burns and M. I. Deselnicu, *Org. Lett.*, 2001, **3**, 2887.
17. S. Chaudhry, S. M. Ryno, M. Zeller, D. R. McMillin, C. Risko and J. Mei, *J. Phys. Chem. B*, 2019, **123**, 3866.
18. A. Capodilupo, F. Manni, G. A. Corrente, G. Accorsi, E. Fabiano, A. Cardone, R. Giannuzzi, A. Beneduci and G. Gigli, *Dyes Pigm.*, 2020, **177**, 108325.
19. C. Lambert and G. Nöll, *J. Am. Chem. Soc.*, 1999, **121**, 8434.
20. M. B. Robin and P. Day, *Adv. Inorg. Chem. Radiochem.*, 1968, **10**, 247.
21. G. A. Corrente, E. Fabiano, F. Manni, G. Chidichimo, G. Gigli, A. Beneduci and A. Capodilupo, *Chem. Mater.*, 2018, **30**, 5610.
22. P. M. Burrezo, W. Zeng, M. Moos, M. Holzapfel, S. Canola, F. Negri, C. Rovira, J. Veciana, H. Phan, J. Wu, C. Lambert and J. Casado, *Angew. Chem. Int. Ed.*, 2019, **41**, 14467.
23. K. Su, N. Sun, Z. Yan, S. Jin, X. Li, D. Wang, H. Zhou, J. Yao and C. Chen, *ACS Appl. Mater. Interfaces*, 2020, **12**, 22099.
24. S. Pluczyk, P. Zassowski, C. Quinton, P. Audebert, V. Alain-Rizzo and M. Lapkowski, *J. Phys. Chem. C*, 2016, **120**, 4382.
25. S. Kim and Y. You, *Adv. Opt. Mater.*, 2019, **7**, 1900201.

26. D. Bessinger, K. Muggli, M. Beetz, F. Auras and T. Bein, *J. Am. Chem. Soc.*, 2021, **143**, 7351.
27. S. Jena and J. Choudhury, *Chem. Commun.*, 2020, **56**, 559.